universe

MDPI

Article

Cosmological Reconstruction and Thermodynamic Analysis of Hybrid Barrow–Ricci Holographic and QCD Ghost Dark Energy

Bhagyashree Chandra [1,2], Ines G. Salako [3,4] and Surajit Chattopadhyay [1,*]

[1] Department of Mathematics, Amity University Kolkata, Major Arterial Road, Action Area II, Rajarhat, New Town, Kolkata 700135, India; bhagyashree.chandra@s.amity.edu
[2] Department of Mathematics, Uluberia College, Uluberia, Howrah 711315, India
[3] Unité de Recherche en Énergies Alternatives et Agriculture de Précision (UR-EAAP), École de Génie Rural (EGR), Université Nationale d'Agriculture (UNA), Kétou 01 BP 55, Benin; ines.salako@imsp-uac.org
[4] Institut de Mathématiques et de Sciences Physiques (IMSP), Université d'Abomey-Calavi (UAC), Porto-Novo 01 BP 613, Benin
* Correspondence: schattopadhyay1@kol.amity.edu or surajitchatto@outlook.com

Abstract

The current study reports a reconstructed dark-energy model combining Barrow holographic Ricci dark energy (BHDE) with QCD ghost dark energy (GDE) in an effective $f(T)$ description. We have examined two prescriptions: an additive BHDE–GDE sector and a correspondence between the two components. Three scale factors, namely hybrid, linear truncation, and quadratic truncation, have been constrained using Cosmic Chronometer (CC) data. We have reconstructed $f(T)$ from the first modified Friedmann equation and evaluated a normalized residual of the second equation. As the pressure has been obtained from the continuity relation, this residual is not an independent consistency test. We have also examined the power-law ansatz $f_{\rm PL}(T) = T + \beta(-T)^m$. Under the adopted source-density normalization, this ansatz has exhibited appreciable field-equation residuals over the relevant redshift range and does not consistently reproduce the prescribed backgrounds. For the reconstructed function, we have evaluated the effective-fluid stability diagnostic and horizon thermodynamics. The adiabatic effective-fluid sound speed has been found to be negative at the present epoch for all three scale factors and developed poles at finite redshift, whereas the horizon entropy-production rate has been positive for the adopted Barrow normalization. These findings are conditional on the reference parameter choices, reconstruction prescription, and diagonal-error likelihood used for the CC data.

Keywords: modified gravity; Barrow entropy; QCD ghost dark energy; holographic Ricci dark energy; generalized second law

Check for updates

Academic Editor: Panayiotis Stavrinos

Received: 6 September 2026
Revised: 24 October 2026
Accepted: 29 October 2026
Published: 3 November 2026

Copyright: © 2026 by the authors. Licensee MDPI, Basel, Switzerland. This article is an open access article distributed under the terms and conditions of the Creative Commons Attribution (CC BY) license.

1. Introduction

Observations of Type Ia supernovae provided the first strong evidence for the late-time accelerated expansion of the universe [1,2]. This acceleration is also supported by measurements of the cosmic microwave background (CMB) anisotropies [3] and baryon acoustic oscillations (BAOs) [4]. Within general relativity, the accelerated expansion is commonly described by an effective component with negative pressure, referred to as dark energy (DE) [5]. Several phenomenological descriptions of dark energy have been proposed. The cosmological constant Λ is the simplest possibility, but its small observed value raises the well-known fine-tuning problem [6]. This has motivated alternatives based on dynamical dark energy and modified gravity [7]. Quintessence models describe a

dynamical component with $w > -1$ [8], whereas phantom models have $w < -1$ and may lead to future singularities such as the Big Rip [9]. Other possibilities include Chaplygin-gas and interacting-dark-energy scenarios [10,11]. Generalized holographic constructions provide another class of models in which modified entropy relations and/or generalized infrared cutoffs are used to describe cosmic acceleration [11–14].

The holographic principle states that the number of degrees of freedom in a gravitating system is bounded by its boundary area [15,16]. Cohen et al. showed that the vacuum energy in an effective field theory is constrained by black hole formation [17], and Li subsequently formulated the holographic dark-energy model in which the infrared cutoff determines the dark-energy density [18]. The choice of infrared cutoff is therefore central to the cosmological dynamics; the Ricci scale provides one alternative to the future event horizon [19,20]. Generalized holographic models extend this construction by modifying the entropy–area relation, the infrared cutoff, or both [13,14,21–23]. These constructions also provide connections to broader cosmological scenarios, including models linking early-time inflation and late-time acceleration [12,24].

Barrow holographic dark energy (BHDE) is obtained by replacing the standard Bekenstein–Hawking entropy–area relation with the Barrow entropy law. Saridakis introduced BHDE using this prescription [25], and subsequent studies have investigated its cosmological dynamics, reconstruction, and observational constraints [26–29]. Unlike Barrow HDE, which modifies the entropy–area relation, Ricci dark energy arises from a generalized choice of the infrared (IR) cutoff. This cutoff is related to the Ricci scalar curvature of spacetime instead of the future event horizon, and the model can also be embedded within the generalized holographic dark-energy (GHDE) framework. del Campo et al. [30] studied holographic dark energy with an infrared cutoff that is proportional to the Ricci scale, including its background dynamics and perturbations in a flat FLRW universe. Fu et al. [31] extended the holographic Ricci model to interacting dark sectors and constrained it using SN Ia, CMB, and BAO data. In contrast to these holographic constructions, QCD ghost dark energy originates from vacuum energy contributions of the Veneziano ghost field in curved spacetime and offers an alternative explanation of cosmic acceleration based on quantum vacuum effects [32].

The accelerated expansion of the universe has also motivated modified-gravity approaches [33,34]. Such theories can reproduce late-time acceleration through modified gravitational dynamics rather than an independently introduced dark-energy component, and their cosmological consequences have been studied using effective equations of state and observational constraints [35,36]. Modified theories of gravity are reviewed comprehensively in Ref. [37]. Later reviews and comparative studies cover extensions such as $f(T)$, $f(R)$, and Gauss–Bonnet gravity, which have been proposed to explain the observed cosmic acceleration and the dynamics of the early universe [10,38–40]. Several viable $f(R)$ models have likewise been developed as alternatives to dark energy [41–44].

Generalized entropy has also been used to study the thermodynamics of gravitational systems and holographic dark-energy models. Within this framework, Jawad et al. [45] examined the stability and thermodynamic geometry of black holes and showed how generalized entropy influences black hole equilibrium and phase transitions. Earlier, Jahromi et al. [46] introduced a new holographic dark-energy model that was derived from the generalized entropy formalism. The Barrow entropy concept was also studied in modified-gravity frameworks; for example, Jawad et al. [47] investigated Barrow holographic dark energy in the setting of deformed Hořava–Lifshitz gravity and found deviations from the standard holographic scenario. Karami and Abdolmaleki investigated the generalized second law (GSL) in $f(T)$ gravity for a spatially flat FLRW universe bounded by the Hubble horizon [48]. Recent work has examined the generalized sec-

ond law (GSL) for Barrow holographic dark-energy models with generalized cutoffs [49]. The GSL requires the total entropy, including the horizon and matter contributions, not to decrease with cosmic time. Earlier, Mathew and Praseetha specifically analyzed the GSL in a universe with holographic Ricci dark energy and found that the generalized second law is satisfied at the apparent horizon under certain conditions [50]. Honarvaryan, Sheykhi and Moradpour studied the thermodynamics of ghost dark energy and its entropy evolution [51]. We use the generalized second law as a thermodynamic test of dark-energy and modified-gravity models.

Ohta introduced the QCD ghost dark-energy mechanism [52], and later studies examined its cosmological evolution and observational viability [32,53]. Garcia-Salcedo et al. [54], however, argued that this model does not reproduce the main features of the standard cosmological paradigm. Our construction is phenomenological and does not resolve that criticism; we use the ghost term only as part of an effective dark sector.

BHDE and GDE have different physical origins, but both have been studied as possible explanations for late-time acceleration. A combined Barrow-entropy and QCD-ghost model was considered by Altaibayeva et al. [55], who studied its background evolution, scalar-field reconstruction, apparent-horizon thermodynamics, and effective-fluid stability. Related studies have also investigated the cosmological evolution and dynamical stability of dark-energy models in modified-gravity frameworks, including $f(Q)$ gravity [56]. This study extends that analysis in three ways. First, we use a Ricci-scale infrared cutoff, making the Barrow holographic density depend on both H and $\dot{H}$. Second, we compare an additive BHDE–GDE density with a prescription that imposes a correspondence between the two components. Third, we study hybrid, linear, and quadratic scale-factor histories constrained by Cosmic Chronometer data and examine their effective equation of state, deceleration parameter, stability diagnostic, Om and Statefinder parameters, and generalized second law. We also reconstruct an effective $f(T)$ function. The combined BHDE–GDE sector is considered here as a phenomenological model. The related work on conformal transformations and modified-gravity representations is discussed in Ref. [57].

The paper is organized as follows. Section 2 presents the model and reconstruction method. Sections 3 and 4 describe the two reconstruction prescriptions and the CC constraints. Sections 5–7 discuss the deceleration parameter, the $f(T)$ reconstruction, and the effective-fluid stability diagnostic. Section 8 presents the Om and Statefinder results, Section 9 examines the generalized second law, and Section 10 compares the three histories. Section 11 gives the conclusions.

2. Theoretical Framework

2.1. Methodological Framework of the Reconstruction

We prescribe the scale factor and reconstruct the associated effective dark-energy quantities. This differs from solving the modified Friedmann equations for a specified gravity theory and matter content. The scale factors are not claimed to be exact solutions of those equations. Instead, they define expansion histories from which we calculate H, R, the effective dark-energy density, the reconstructed equation of state, and the deceleration parameter.

We work in a spatially flat Friedmann–Lemaître–Robertson–Walker (FLRW) universe, consistent with the standard large-scale cosmological description supported by supernova, CMB, and BAO observations [1,2,4,58]. We first define the hybrid model containing Barrow holographic dark energy and QCD ghost dark energy.

For the spatially flat FLRW metric [59,60]

$$ds^2 = -dt^2 + a^2(t)\,(dx^2 + dy^2 + dz^2), \tag{1}$$

the Ricci scalar R is given by

$$R = 6\left(\dot{H} + 2H^2 + \frac{k}{a^2}\right). \tag{2}$$

Since we consider a flat geometry ($k = 0$), this reduces to

$$R = 6\left(\dot{H} + 2H^2\right), \tag{3}$$

As noted in the Introduction, the holographic principle states that the degrees of freedom of a physical system scale with its boundary area rather than its volume [15,16]. Cohen et al. [17] showed that the quantum zero-point energy of a system must be bounded to avoid black hole formation, which led Li to formulate holographic dark energy (HDE) [18].

In Barrow entropy, the standard Bekenstein–Hawking area law $S \propto A$ [61,62] is generalized to a fractal-like deformation of the horizon surface $S \propto A^{1+\Delta/2}$ [63], where the Barrow exponent Δ encodes the degree of quantum-gravitational deformation ($0 \leq \Delta \leq 1$) and $\Delta = 0$ recovers the classical area law. The deformation is attributed to possible quantum-gravitational effects on the geometry of the horizon surface [25,63].

Using this entropy modification, the corresponding holographic dark-energy density takes the generalized scaling form [23,25,63]

$$\rho_{\mathrm{BHDE}} \propto L^{\Delta-2}, \qquad 0 < \Delta < 1 \tag{4}$$

where L is the infrared (IR) cutoff. Such generalized holographic models have been investigated as a way of incorporating quantum-gravity corrections into cosmology [13,64].

The choice of the infrared cutoff scale is central to holographic dark-energy models. The future event horizon is often used, but it suffers from causality issues [19]. The Ricci scalar curvature has been proposed as an alternative, leading to the Ricci dark-energy model [20]. Here the infrared cutoff is dynamically related to the spacetime curvature, so the dark-energy density is directly tied to the cosmic expansion. Shekh et al. [65] demonstrated the physical acceptability of Rényi, Tsallis, and Sharma–Mittal holographic dark-energy models in $f(T, B)$ gravity under the Hubble cutoff, providing a useful reference for assessing the viability of entropy-modified holographic dark-energy models.

Following Ref. [53], we write the ghost dark-energy (GDE) density as

$$\rho_{GDE} = \alpha H, \tag{5}$$

with $\alpha \sim \Lambda^3_{\mathrm{QCD}}$. The origin of ghost dark energy lies in the Veneziano ghost field in quantum chromodynamics (QCD), which contributes to the vacuum energy in curved spacetime but vanishes in flat spacetime [52,66]. The Veneziano ghost contribution therefore supplies a vacuum-energy term without introducing an additional propagating degree of freedom.

We consider a hybrid effective dark-energy sector containing both Barrow holographic dark energy and QCD ghost dark energy. The two components have different physical origins: BHDE incorporates the Barrow modification of the entropy–area relation, whereas GDE is associated with QCD vacuum effects. We combine them to study the background dynamics in a common effective description.

2.2. Physical Significance of the Hybrid Model

The hybrid construction is useful for testing how the Barrow deformation modifies the cosmological dynamics in the presence of the QCD ghost contribution. We do not assume

that the combined model is automatically stable; stability is assessed separately through the effective-fluid squared sound speed, while thermodynamic consistency is tested through the generalized second law.

3. Reconstruction of the EoS Parameter

3.1. Approach I: DE Density Is Taken as Sum of BHDE and GDE

3.1.1. Additive BHDE–GDE Construction

In Approach I, we take the effective dark-energy density to be $\rho_{DE} = \rho_{BHDE} + \rho_{GDE}$. This additive construction combines the Barrow entropy correction in the holographic sector with the QCD ghost contribution $\rho_{GDE} = \alpha H$. It allows us to examine how the Barrow deformation parameter Δ affects the reconstructed cosmological evolution when both contributions are present.

3.1.2. Implementation of Ricci Scale as Infrared Cutoff and EoS Reconstruction

In this case, we use the Ricci length as the infrared (IR) cutoff, $L = (R/6)^{-1/2}$, rather than identifying the length L directly with the Ricci scalar R. For a spatially flat FLRW universe, the Ricci scalar is expressed as [59,60]

$$R = 6(\dot{H} + 2H^2), \tag{6}$$

where H is the Hubble parameter and a dot denotes differentiation with respect to cosmic time. The Ricci length L connects the holographic dark-energy density to the dynamical curvature of the universe.

Based on this chosen form of IR cutoff, the holographic Ricci dark-energy (HRDE) density takes the form [20,30]

$$\rho_{HDE} = 3c^2(\dot{H} + 2H^2), \tag{7}$$

so that the dark-energy density depends on both the expansion rate and its time derivative.

On the other hand, the general expression of holographic dark energy (HDE) is given by [17,18]

$$\rho_{HDE} = 3c^2 M_p^2 L^{-2} = 3c^2 L^{-2}, \tag{8}$$

where c is a dimensionless parameter controlling the strength of holographic contribution, $M_p^2 = 1$ is the reduced Planck mass (in natural units), and L represents the IR cutoff length scale.

By comparing Equations (7) and (8), we obtain the relation

$$L = (\dot{H} + 2H^2)^{-1/2}. \tag{9}$$

This relation shows that the infrared scale is dynamically determined by the cosmic expansion history.

Generalized entropy constructions provide a broader framework in which modified entropy–area relations can enter holographic dark-energy models [64,67]. For the numerical analysis, we use quantities normalized to the present Hubble scale and set $H_0 = 1$. We write $\bar{R} = R/H_0^2$ for the dimensionless Ricci scalar and $\bar{\rho}_{BHDE} = \rho_{BHDE}/(M_{\rm Pl}^2 H_0^2)$ for the dimensionless density. The Ricci cutoff is $L^{-2} = R/6$, so its dimensionless version obeys $\bar{L}^{-2} = \bar{R}/6$. In this convention, the exact Barrow–Ricci scaling is

$$\bar{\rho}_{BHDE} = 3c^2 \bar{L}^{\Delta-2} = \frac{c^2}{2} 6^{\Delta/2} \bar{R}^{1-\Delta/2}. \tag{10}$$

Here, Δ is the Barrow deformation parameter. The dimensionful expression corresponding to this normalization is $\rho_{BHDE} = (c^2/2)6^{\Delta/2} M_{\rm Pl}^2 H_0^{\Delta} R^{1-\Delta/2}$.

In this section, we set $H_0 = 1$. Time, the Hubble parameter, the Ricci scalar, and the energy densities are expressed in units of H_0^{-1}, H_0, H_0^2, and $M_{\rm Pl}^2 H_0^2$, respectively. We define the dimensionless Ricci scalar as $\bar{R} = R/H_0^2$; with $H_0 = 1$, this is the numerical quantity used in the background expressions. For the numerical prescription, we expand the curvature-dependent factor $\bar{R}^{-\Delta/2}$ to first order in Δ while retaining the normalization factor $6^{\Delta/2}$ exactly:

$$\bar{\rho}_{BHDE} \approx \frac{c^2}{2} 6^{\Delta/2} \left(\bar{R} - \frac{\Delta}{2} \bar{R} \ln \bar{R} \right). \tag{11}$$

Here and below, the logarithm is always applied to the dimensionless quantity $\bar{R}$; we do not take the logarithm of a dimensional curvature. This real-valued expansion is used only on intervals where $\bar{R} > 0$; parameter/time regions with non-positive Ricci scalars lie outside the domain of this prescription. The same normalization is used in the explicit scale-factor cases and the reconstruction residual calculation. At $\Delta = 0$, this convention gives $\rho_{\rm BHDE} = 3c^2 L^{-2} = c^2 R/2$ because $R = 6L^{-2}$. Thus, the coefficient multiplying R is $c^2/2$ rather than $3c^2$ because the factor of six is absorbed by the relation between R and L^{-2}. In dimensional expressions at nonzero Δ, the factor H_0^{Δ} restores the density dimensions, while the numerical reconstruction uses $H_0 = 1$.

In Approach I, the effective dark-energy sector is taken as the sum of BHDE and GDE:

$$\rho_{DE} = \rho_{BHDE} + \rho_{GDE}.$$

After we include the matter contribution, the total effective energy density of the universe becomes

$$\rho_{eff} = \rho_{BHDE} + \rho_{GDE} + \rho_{m0} a^{-3},$$

where the component densities are expressed in the same $H_0 = 1$ normalized units and ρ_{m0} is the present normalized matter density.

Substituting the component densities, the total effective density becomes

$$\rho_{eff} = \frac{c^2}{2} 6^{\Delta/2} \left(\bar{R} - \frac{\Delta}{2} \bar{R} \ln \bar{R} \right) + \alpha H + \rho_{m0} a^{-3}. \tag{12}$$

The total effective density includes both the dark-energy sector and pressureless matter.

The parameter c sets the strength of the holographic contribution. The constant α describes the QCD ghost term and is related to the QCD scale by $\alpha \sim \Lambda_{\rm QCD}^3$. The parameters ψ and n control the exponential and power-law parts of the hybrid scale factor.

Differentiating Equation (12) with respect to the normalized time variable (using $H_0 = 1$), we obtain

$$\dot{\rho}_{\rm eff} = 3c^2 6^{\Delta/2} (\ddot{H} + 4H\dot{H}) \left[1 - \frac{\Delta}{2} \{ 1 + \ln \bar{R} \} \right] + \alpha \dot{H} - 3\rho_{m0} H a^{-3}. \tag{13}$$

The time derivative of the effective density depends on $\ddot{H}$ and therefore the detailed time evolution of the prescribed expansion history.

Since pressureless matter is separately conserved, $\dot{\rho}_m = -3H\rho_m$, the dark-energy density obeys

$$\dot{\rho}_{DE} = \dot{\rho}_{\rm eff} + 3H\rho_m = \dot{\rho}_{\rm eff} + 3H\rho_{m0} a^{-3}. \tag{14}$$

Assuming that the BHDE–GDE sector is separately conserved, its EoS parameter is

$$w_{DE} = -1 - \frac{\dot{\rho}_{DE}}{3H\rho_{DE}}. \tag{15}$$

Applying the continuity form to the total effective fluid, the reconstructed total-fluid EoS parameter is defined as

$$w_{\text{reconst}} = -1 - \frac{\dot{\rho}_{eff}}{3H\rho_{eff}}. \tag{16}$$

Substituting Equations (12) and (13) into the above expression, we obtain the total-fluid EoS in explicit form:

$$w_{\text{reconst}} = -1 - \frac{3c^2 6^{\Delta/2}(\ddot{H} + 4H\dot{H})\left[1 - \frac{\Delta}{2}\{1 + \ln \bar{R}\}\right] + \alpha\dot{H} - 3\rho_{m0}Ha^{-3}}{3H\left\{\frac{c^2}{2}6^{\Delta/2}\left[\bar{R} - \frac{\Delta}{2}\bar{R}\ln\bar{R}\right] + \alpha H + \rho_{m0}a^{-3}\right\}}. \tag{17}$$

Thus, w_{DE} characterizes the dark-energy sector, whereas w_{reconst} characterizes the combined dark-energy and matter fluid. They must be interpreted separately.

Throughout, $\bar{R} \equiv R/H_0^2 = 6(\dot{H} + 2H^2)$ denotes the dimensionless Ricci scalar. As we can see, Equation (12) contains $\ln \bar{R}$. The reconstruction is well defined only for $\bar{R} > 0$; i.e., $\dot{H} + 2H^2 > 0$. This condition holds during the matter-dominated and accelerating epochs considered here. However, it fails in an exactly radiation-dominated phase where $R = 0$. We therefore restrict our analysis to the post-radiation late-time evolution of the universe. The holographic contribution in Equation (12) is also understood as the leading-order expansion in Δ of $\bar{R}^{\,1-\Delta/2}$, so it is valid for small Δ only.

Note that Equations (12)–(17) are obtained from the prescribed scale factor $a(t)$ alone and no field equation is solved at this stage. Consequently, w_{reconst} is a kinematic reconstruction of the total effective fluid. It coincides with the dynamical expression $w = -1 - 2\dot{H}/(3H^2)$ only if ρ_{eff} in Equation (12) also satisfies the Friedmann constraint $\rho_{\text{eff}} \propto H^2$. Finally, $\rho_{\text{eff}} > 0$ is required for w_{reconst} in Equation (17) to remain finite since the denominator vanishes if $\rho_{\text{eff}} = 0$.

3.2. Explicit Form of $W_{Reconst}$ for the Three Reconstructed Scale Factors

Equation (17) is general for the prescribed background. We now substitute the three scale-factor histories to obtain the corresponding explicit expressions for H, $\dot{H}$, $\ddot{H}$, and w_{reconst}.

3.2.1. Motivation for the Choice of Scale Factors

We consider three scale-factor histories to compare the full hybrid form with its first- and second-order truncations. The hybrid form contains both exponential and power-law behavior, while the linear and quadratic forms retain successively higher orders of the exponential expansion. This comparison tests how sensitive the reconstructed dynamics are to the order of truncation.

3.2.2. Case I: $a(t) = e^{\psi\ t}t^n$

We first consider the hybrid scale factor

$$a(t) = e^{\psi t}t^n \tag{18}$$

The hybrid form combines power-law behavior at early times with exponential behavior at late times. For $n > 0$ and $\psi > 0$, the corresponding Hubble parameter evolves from a

power-law-dominated regime toward the constant value ψ, providing a phenomenological transition from deceleration to accelerated expansion.

For this scale factor, the Hubble parameter is

$$H = \frac{\dot{a}}{a} = \psi + \frac{n}{t}. \tag{19}$$

Its first two time derivatives are

$$\dot{H} = -\frac{n}{t^2} \tag{20}$$

and

$$\ddot{H} = \frac{2n}{t^3} \tag{21}$$

respectively. For $n > 0$, $\dot{H} < 0$, so the Hubble parameter decreases monotonically with cosmic time. Substituting H and $\dot{H}$ gives

$$\dot{H} + 2H^2 = 2\psi^2 + \frac{4\psi n}{t} + \frac{2n^2 - n}{t^2}, \tag{22}$$

which explicitly shows contributions from constant, inverse-time, and inverse-square-time terms.

Substitution of $\dot{H} + 2H^2$ into Equation (6) gives

$$R = \frac{6\left(-n + 2(n + t\psi)^2\right)}{t^2} \tag{23}$$

Now, inserting the expressions of the scale factor a, Hubble parameter H, and Ricci scalar R into Equation (12), the effective energy density in Case I is

$$\bar{\rho}_{\text{eff}}(t) = \frac{c^2}{2} 6^{\Delta/2} \bar{R}(t) \left[1 - \frac{\Delta}{2} \ln \bar{R}(t)\right] + \bar{\alpha}\left(\psi + \frac{n}{t}\right) + \bar{\rho}_{m0} e^{-3\psi t} t^{-3n}. \tag{24}$$

and, from Equation (13), the time derivative of effective energy density in Case I is

$$\begin{aligned} \dot{\rho}_{\text{eff}} = {} & 3c^2 6^{\Delta/2} \left[\frac{2n(1-2n)}{t^3} - \frac{4\psi n}{t^2}\right] \times \left[1 - \frac{\Delta}{2}\{1 + \ln \bar{R}(t)\}\right] - \frac{\alpha n}{t^2} \\ & - 3\rho_{m0} H e^{-3\psi t} t^{-3n}. \end{aligned} \tag{25}$$

Substituting a, ρ_{eff}, and $\dot{\rho}_{eff}$ from Equations (18), (24) and (25), respectively, gives the reconstructed EoS parameter for Case I:

$$w_{\text{reconst}}(t) = -1 - \frac{3c^2 6^{\Delta/2}\left[\frac{2n(1-2n)}{t^3} - \frac{4\psi n}{t^2}\right]\left[1 - \frac{\Delta}{2}\{1 + \ln \bar{R}(t)\}\right] - \frac{\alpha n}{t^2} - 3\rho_{m0} H e^{-3\psi t} t^{-3n}}{3H\left[\frac{c^2}{2} 6^{\Delta/2}\left\{\bar{R}(t) - \frac{\Delta}{2}\bar{R}(t)\ln \bar{R}(t)\right\} + \alpha H + \rho_{m0} e^{-3\psi t} t^{-3n}\right]}. \tag{26}$$

The reconstructed w_{reconst} in Equation (26) represents the combined effective fluid that includes the pressureless-matter contribution, and it does not represent the dark-energy component alone. Therefore, if $w_{\text{reconst}} < -1$, it indicates phantom-like behavior of the total effective fluid under the present definition, but it does not directly imply phantom behavior of dark energy alone. Further, the late-time behavior of the universe should be checked from the Hubble parameter $H(t) = \psi + n/t$. For $(\psi > 0)$, we have $H(t) \to \psi$ as $t \to \infty$. This limiting behavior indicates that the expansion rate approaches a constant value. Hence, the de Sitter behavior comes from the evolution of $H(t)$ and not only from the value of w_{reconst}.

3.2.3. Case II: $a(t) = (1+\psi t)t^n$

We next consider the linearly truncated scale factor

$$a(t) = (1+\psi t)t^n. \tag{27}$$

It is obtained by retaining the linear term in the expansion of the exponential factor. The Hubble parameter is

$$H = \frac{\psi}{1+\psi t} + \frac{n}{t}. \tag{28}$$

The first two time derivatives are

$$\dot{H} = -\frac{\psi^2}{(1+\psi t)^2} - \frac{n}{t^2}, \tag{29}$$

and

$$\ddot{H} = \frac{2\psi^3}{(1+\psi t)^3} + \frac{2n}{t^3} \tag{30}$$

respectively.

Substitution of $\dot{H} + 2H^2$ into Equation (6) gives

$$R(t) = 6\left[-\frac{\psi^2}{(1+\psi t)^2} - \frac{n}{t^2} + 2\left(\frac{\psi}{1+\psi t} + \frac{n}{t}\right)^2\right]. \tag{31}$$

Now, inserting the expressions of the scale factor a, Hubble parameter H, and Ricci scalar R from (27), (28) and (31), respectively, into Equation (12), the effective energy density in Case II is

$$\bar{\rho}_{\rm eff}(t) = \frac{c^2}{2}6^{\Delta/2}\bar{R}(t)\left[1 - \frac{\Delta}{2}\ln\bar{R}(t)\right] + \bar{\alpha}\left(\frac{\psi}{1+\psi t} + \frac{n}{t}\right) + \bar{\rho}_{m0}(1+\psi t)^{-3}t^{-3n}. \tag{32}$$

and, from Equation (13), the time derivative of effective energy density in Case II is

$$\begin{aligned}\dot{\rho}_{\rm eff} = {} & 3c^2 6^{\Delta/2}\left[\frac{2\psi^3}{(1+\psi t)^3} + \frac{2n}{t^3} - 4\left(\frac{\psi}{1+\psi t} + \frac{n}{t}\right)\left(\frac{\psi^2}{(1+\psi t)^2} + \frac{n}{t^2}\right)\right] \\ & \times\left[1 - \frac{\Delta}{2}\{1+\ln\bar{R}(t)\}\right] - \alpha\left[\frac{\psi^2}{(1+\psi t)^2} + \frac{n}{t^2}\right] - 3\rho_{m0}\left(\frac{\psi}{1+\psi t} + \frac{n}{t}\right)(1+\psi t)^{-3}t^{-3n}.\end{aligned} \tag{33}$$

The Barrow deformation changes the time dependence of the effective density through the Ricci-dependent term.

Substitution of H, ρ_{eff}, and $\dot{\rho}_{eff}$ from Equations (28), (32) and (33) gives

$$\begin{aligned} w_{\rm reconst,case2}(t) = {} & -1 - \\ & \frac{\begin{array}{l} 3c^2 6^{\Delta/2}\left[\frac{2\psi^3}{(1+\psi t)^3} + \frac{2n}{t^3} - 4\left(\frac{\psi}{1+\psi t} + \frac{n}{t}\right)\left(\frac{\psi^2}{(1+\psi t)^2} + \frac{n}{t^2}\right)\right] \\ \times\left[1 - \frac{\Delta}{2}\{1+\ln\bar{R}(t)\}\right] - \alpha\left[\frac{\psi^2}{(1+\psi t)^2} + \frac{n}{t^2}\right] \\ - 3\rho_{m0}\left(\frac{\psi}{1+\psi t} + \frac{n}{t}\right)(1+\psi t)^{-3}t^{-3n} \end{array}}{3\left(\frac{\psi}{1+\psi t} + \frac{n}{t}\right)\left[\frac{c^2}{2}6^{\Delta/2}R(t)\left(1 - \frac{\Delta}{2}\ln\bar{R}(t)\right)\right.} \\ & \left. + \alpha\left(\frac{\psi}{1+\psi t} + \frac{n}{t}\right) + \rho_{m0}(1+\psi t)^{-3}t^{-3n}\right] \end{aligned}. \tag{34}$$

At early times, $t \to 0$, the inverse powers of t may cause rapid changes in the reconstructed total-fluid EoS $w_{\rm tot} = w_{\rm reconst}$. Whether its value is below or above -1, it describes the

behavior of the combined fluid. Therefore, we cannot directly infer that dark energy is phantom-like or quintessence-like without calculating its EoS separately. At late times, the value of w_{tot} depends on the chosen density expression and scale factor. Hence, the value of w_{tot} alone is not sufficient to conclude that the universe approaches a de Sitter phase.

3.2.4. Case III: $a(t) = \left(1 + \psi t + \frac{\psi^2 t^2}{2}\right) t^n$

We next consider the quadratically truncated hybrid scale factor

$$a(t) = \left(1 + \psi t + \frac{\psi^2 t^2}{2}\right) t^n, \tag{35}$$

which corresponds to retaining terms up to second order in the series expansion of the exponential factor. This form retains the next term in the exponential expansion. We define

$$F(t) = 1 + \psi t + \frac{\psi^2 t^2}{2}, \tag{36}$$

so that the scale factor can be written compactly as $a(t) = F(t)t^n$. With this definition, the Hubble parameter becomes

$$H = \frac{\dot{F}}{F} + \frac{n}{t} = \frac{\psi + \psi^2 t}{F} + \frac{n}{t}. \tag{37}$$

The first- and second-order time derivatives of the Hubble parameter are accordingly obtained as

$$\dot{H} = \frac{\psi^2 F - (\psi + \psi^2 t)^2}{F^2} - \frac{n}{t^2}. \tag{38}$$

and

$$\ddot{H} = \frac{2\left(-4t^3\psi^3 + 6t^5\psi^5 + 2t^6\psi^6 + n[2 + t\psi(2 + t\psi)]^3\right)}{t^3[2 + t\psi(2 + t\psi)]^3} \tag{39}$$

respectively. The rational form of the scale factor determines the corresponding time dependence of H. For positive ψ and n, the second term remains negative, and the overall behavior corresponds to a decreasing Hubble rate with cosmic time.

Substitution of $\dot{H} + 2H^2$ into Equation (6) gives

$$R(t) = 6\left[\frac{-\psi^3 t - \frac{\psi^4 t^2}{2}}{\left(1 + \psi t + \frac{\psi^2 t^2}{2}\right)^2} - \frac{n}{t^2} \quad + 2\left(\frac{\psi + \psi^2 t}{1 + \psi t + \frac{\psi^2 t^2}{2}} + \frac{n}{t}\right)^2\right]. \tag{40}$$

Using Equations (35), (37) and (40) in Equation (12), the effective density in Case III is

$$\bar{\rho}_{\text{eff}}(t) = \frac{c^2}{2} 6^{\Delta/2} \bar{R}(t)\left[1 - \frac{\Delta}{2}\ln \bar{R}(t)\right] + \bar{\alpha}\left[\frac{\psi + \psi^2 t}{1 + \psi t + \frac{\psi^2 t^2}{2}} + \frac{n}{t}\right] + \bar{\rho}_{m0}\left(1 + \psi t + \frac{\psi^2 t^2}{2}\right)^{-3} t^{-3n}, \tag{41}$$

and, from Equation (13), the time derivative of effective energy density in Case III is

$$\begin{aligned}\dot{\rho}_{\rm eff} = 3c^2 6^{\Delta/2}\Bigg[&-\frac{3\psi^3(1+\psi t)}{F^2}+\frac{2\psi^3(1+\psi t)^3}{F^3}+\frac{2n}{t^3}\\ &-4\left(\frac{\psi+\psi^2 t}{F}+\frac{n}{t}\right)\left(\frac{\psi^3 t+\frac{\psi^4 t^2}{2}}{F^2}+\frac{n}{t^2}\right)\Bigg]\left[1-\frac{\Delta}{2}\{1+\ln\bar{R}(t)\}\right]\\ &+\alpha\left[\frac{\psi^2 F-(\psi+\psi^2 t)^2}{F^2}-\frac{n}{t^2}\right]\\ &-3\rho_{m0}\left(\frac{\psi+\psi^2 t}{F}+\frac{n}{t}\right)F^{-3}t^{-3n}.\end{aligned} \tag{42}$$

The quadratic truncation modifies the Ricci-dependent contribution to the effective dark-energy density.

Substituting H, ρ_{eff}, and $\dot{\rho}_{eff}$ from Equations (37), (41) and (42) gives the reconstructed EoS for Case III,

$$w_{\rm reconst,case3}(t) = -1-\frac{\mathcal{N}(t)}{3t^2\mathcal{A}^4(t)\mathcal{B}(t)\mathcal{D}(t)}, \tag{43}$$

where the expressions in the denominator of Equation (43) are

$$\mathcal{A}(t) = 2+t\psi(2+t\psi), \tag{44}$$

$$\mathcal{B}(t) = n+\frac{2t\psi(1+t\psi)}{2+t\psi(2+t\psi)}, \tag{45}$$

and

$$\begin{aligned}\mathcal{D}(t) = &\frac{16t^{-3n}\rho_{m0}}{\mathcal{A}^3(t)}+\frac{2\alpha\mathcal{B}(t)}{t}\\ &+\frac{2^{\Delta/2}3^{1+\Delta/2}c^2\mathcal{C}(t)\left[2-\Delta\ln\left(\frac{6\mathcal{C}(t)}{t^2\mathcal{A}^2(t)}\right)\right]}{t^2\mathcal{A}^2(t)},\end{aligned} \tag{46}$$

with

$$\begin{aligned}\mathcal{C}(t) = &-2t^3\psi^3(2+t\psi)+2\Big[2n+2(1+n)t\psi+(2+n)t^2\psi^2\Big]^2\\ &-n\mathcal{A}^2(t).\end{aligned} \tag{47}$$

The numerator in Equation (43) is given by

$$\begin{aligned}\mathcal{N}(t) = t^{-3n}\Big\{2t\Big[&24t\rho_{m0}\big(-2t\psi(1+t\psi)-n\mathcal{A}\big)\\ &-t^{3n}\alpha\mathcal{A}^2\big(2t^3\psi^3(2+t\psi)+n\mathcal{A}^2\big)\Big]\\ &+t^{3n}\,6^{1+\Delta/2}c^2\,\mathcal{A}\,\mathcal{E}\left[(\Delta-2)+\Delta\ln\frac{6\mathcal{C}}{t^2\mathcal{A}^2}\right]\Big\}.\end{aligned} \tag{48}$$

with

$$\begin{aligned}\mathcal{E}(t) = &\,2n^2\mathcal{A}^3(t)+2t^3\psi^3(1+t\psi)[2+3t\psi(2+t\psi)]\\ &+n\mathcal{A}(t)\Big[-4+t^2\psi^2(8+t\psi(16+7t\psi))\Big].\end{aligned} \tag{49}$$

3.3. Observational Constraints from Cosmic Chronometer Data

For the observational analysis, we introduce the dimensionless parameter $p = \psi t_0$, where ψ appears in the scale-factor parameterizations and t_0 is the present cosmic time. The parameters (H_0, p, n) are determined separately for each parameterization using the 32 Cosmic Chronometer (CC) measurements compiled by Favale, Gómez-Valent and

Migliaccio [68] over $0.07 \leq z \leq 1.965$. The observed $H(z)$ values and quoted uncertainties are taken from Table 1 of Ref. [68]. In the fits reported here, we use the diagonal chi-square

$$\chi^2_{\rm CC}(\boldsymbol{\theta}) = \sum_{i=1}^{32} \frac{[H_{\rm th}(z_i;\boldsymbol{\theta}) - H_i]^2}{\sigma_i^2}, \qquad \boldsymbol{\theta} = (H_0, p, n), \tag{50}$$

where H_i and σ_i are the tabulated central values and individual quoted uncertainties. Thus, this likelihood treats the measurements as uncorrelated; it does not include the available non-diagonal systematic covariance for subsets of the compilation. The fit and the flat ΛCDM comparison shown in Figure 1 use this same diagonal-error prescription. The reported information criteria are therefore conditional on this choice of likelihood.

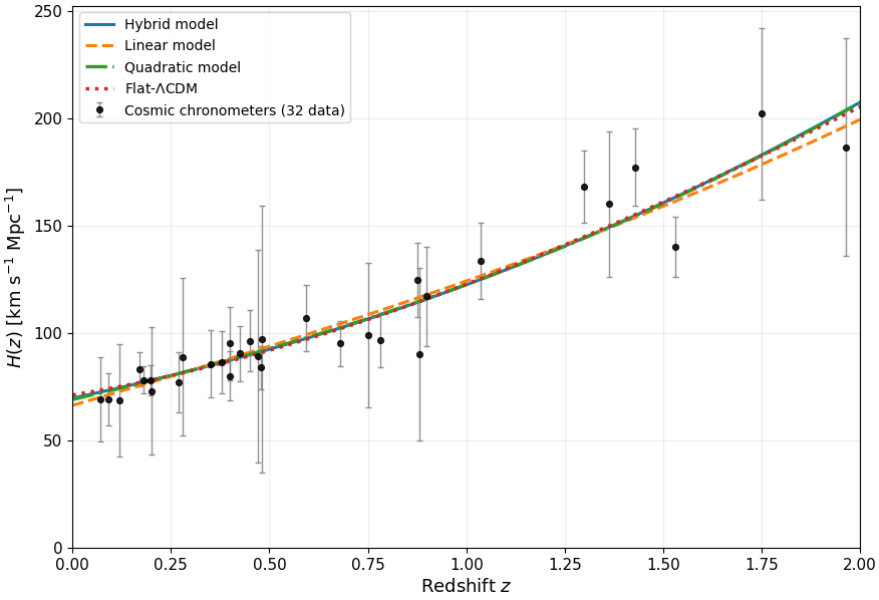


Figure 1. Theoretical Hubble parameter $H(z)$ for the hybrid, linearly truncated and quadratically truncated scale-factor models, together with the best-fit flat ΛCDM curve, compared with the 32 Cosmic Chronometer (CC) measurements. The flat ΛCDM parameters are fitted to the same data using the diagonal chi-square defined in Equation (50); the error bars show the individual quoted uncertainties. Correlations in the systematic covariance are not included in these fits.

For each parameterization the model prediction is $H_{\rm th}(z; H_0, p, n) = H_0\,\tilde{H}(x)/\tilde{H}(1)$, where $x = t/t_0$, $\tilde{H}(x) = d\ln a/dx$ is the Hubble rate in units of t_0^{-1} and $x(z)$ is the root of $a(x)/a(1) = (1+z)^{-1}$. Explicitly, $\tilde{H} = p + n/x$ (hybrid), $\tilde{H} = p/(1+px) + n/x$ (linear), and $\tilde{H} = (p + p^2x)/F(x) + n/x$ with $F(x) = 1 + px + p^2x^2/2$ (quadratic). The values $\chi^2_{\rm red} \simeq 0.4 < 1$ indicate that the quoted diagonal uncertainties are conservative relative to the scatter of the data; they are not rescaled here.

For reference, flat ΛCDM is fitted independently to the same 32 CC points using Equation (50) with $H_{\Lambda\rm CDM}(z) = H_0[\Omega_{m0}(1+z)^3 + 1 - \Omega_{m0}]^{1/2}$. The diagonal-error fit gives $H_0 = 71.0291$ km s^{-1} Mpc^{-1} and $\Omega_{m0} = 0.28261$ with $\chi^2_{\rm min} = 11.6554$ and $\chi^2_{\rm red} = 0.3885$. This is a separate flat ΛCDM fit and does not refit the three kinematic models.

In addition to minimizing $\chi^2_{\rm CC}$, we sampled the parameter posterior for each scale-factor prescription using a Markov Chain Monte Carlo (MCMC) procedure. The likelihood was taken to be proportional to $\exp\left[-\chi^2_{\rm CC}/2\right]$; $\chi^2_{\rm CC}$ is defined in Equation (50). Hence, as in the best-fit analysis, the quoted CC errors were treated as diagonal, and non-diagonal systematic covariance was not included. The corner plots in Figure 2 show the marginalized posterior distributions of (H_0, p, n) along the diagonal and their joint distributions off the

diagonal. The dashed vertical lines mark the 16th, 50th, and 84th percentiles; the median and the 16th/84th percentiles summarize the parameter estimates and their central 68% credible intervals. The joint contours illustrate parameter correlations and degeneracies.

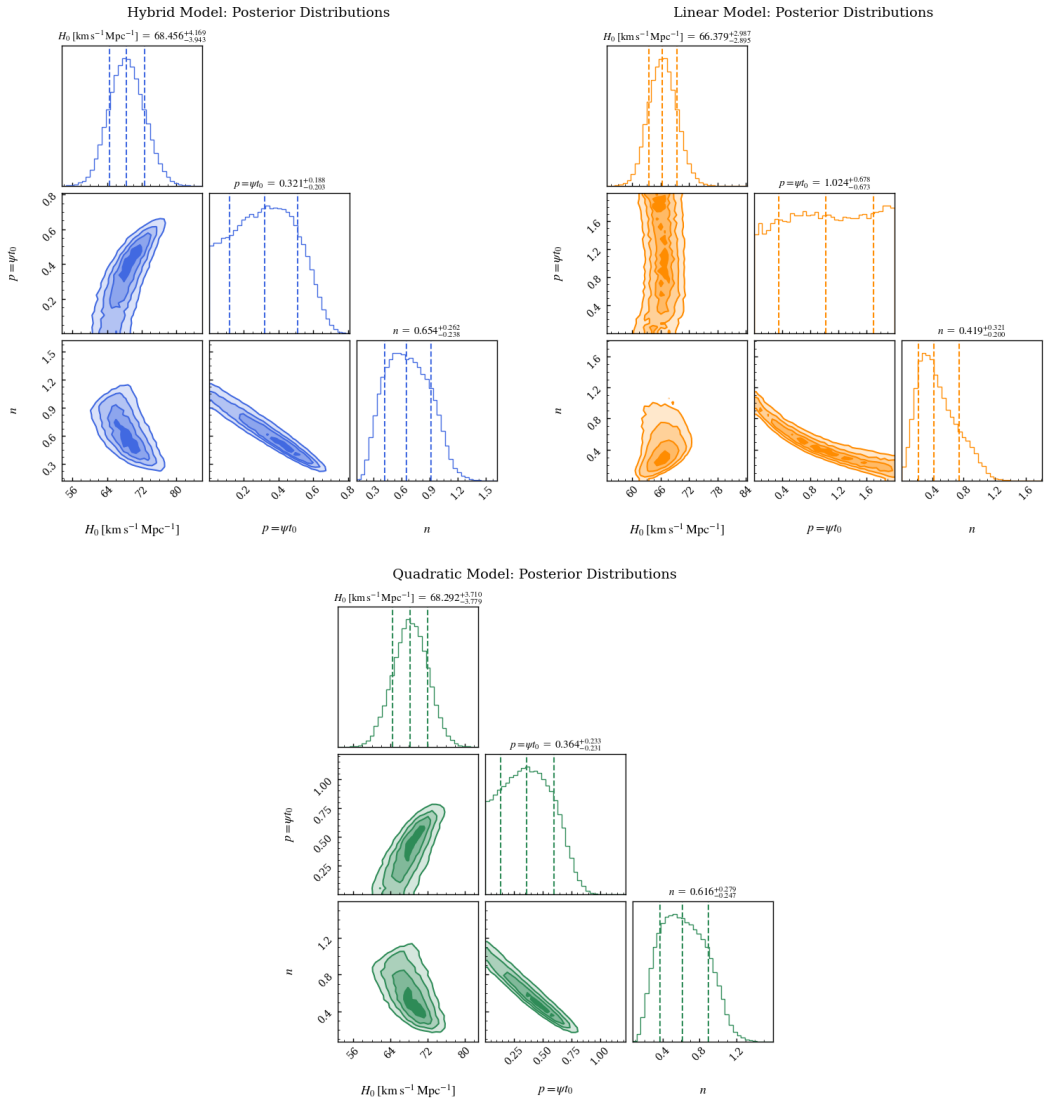


Figure 2. MCMC corner plots for the (**blue**) hybrid, (**orange**) linearly truncated, and (**green**) quadratically truncated scale-factor models that were obtained using the 32-point Cosmic Chronometer $H(z)$ dataset. The diagonal panels show the marginalized posterior distributions of H_0, $p = \psi t_0$, and n, while the off-diagonal panels show their joint posterior distributions and parameter correlations. Dashed vertical lines indicate the 16th, 50th, and 84th percentiles of each marginalized posterior, with the 16th and 84th percentiles defining the central 68% credible interval.

The posterior summaries indicate that the inferred values of H_0 are broadly concentrated around 66–69 km s^{-1} Mpc^{-1} across the three prescriptions. The joint contours also show parameter degeneracies, most clearly the negative correlation between p and n. In the linear model, the marginalized posterior for p is comparatively broad and rises towards the upper end of the displayed parameter range. The likelihood, fitted parameter vector, data compilation, and diagonal-error treatment are specified above; the posterior contours are interpreted as conditional on the sampling ranges used to generate the displayed chains.

Throughout the numerical analysis, we use natural units and express dimensionful quantities in units set by the present Hubble scale. The CC likelihood gives separate estimates of (H_0, p, n) for each scale-factor history. The numerical analysis uses $c = 1.2$,

$\Omega_{m0} = 0.30$, and $\Delta = 0.10, 0.15, 0.20$. These are fiducial choices for the reconstruction, not jointly constrained parameters by the CC-only fit: $c = 1.2$ is held fixed to isolate the effect of varying the Barrow deformation parameter, while $\Omega_{m0} = 0.30$ is a representative present-day matter fraction. The values $\Delta = 0.10, 0.15, 0.20$ sample a modest range of nonzero Barrow deformations. The curves show the dependence on Δ over the relevant range; a broader parameter study is left for future work. In the power-law ansatz $f_{\rm PL}(T) = T + \beta(-T)^m$, we fix $m = 0.32$ as a phenomenological test value and determine β from the present-day normalization; m is not fitted to the CC data, and the residual conclusions for this ansatz are conditional on this choice. In the adopted H_0-normalized convention, the dimensionless matter density is $\rho_m = 3\Omega_{m0}(1+z)^3$ and the ghost term used in the residual calculation is $\rho_{\rm GDE} = 4.32E$, where $E = H/H_0$ and $4.32 = 3c^2$. The same source-density prescription is used for all three backgrounds. The numerical residuals should be read within this convention; the dimensional quantities must be converted consistently if physical units are restored. The Barrow entropy normalization γ is kept explicit. The CC-fit variable $x = t/t_0$ and the function $\widetilde{H}(x)$ are dimensionless. We recover the physical Hubble rate from $H(t) = H_0\widetilde{H}(x)/\widetilde{H}(1)$. In plots with $H_0 = 1$, we use $\tau = H_0 t$; physical time is then $t = \tau/H_0$. If H_0 is given in km s^{-1} Mpc^{-1}, then $H_0^{-1} = 977.8/[H_0/(\mathrm{km\,s^{-1}\,Mpc^{-1}})]$ Gyr. For example, $H_0 = 70\,\mathrm{km\,s^{-1}\,Mpc^{-1}}$ gives $H_0^{-1} \simeq 13.97$ Gyr. The CC fit and Approach II use different time origins, as specified in those sections.

Before closing this subsection, let us note that, for the quadratic model, the normalized Hubble parameter is defined such that $H_{\rm th}(0) = H_0$. Using the best-fit parameters in Table 1, this gives $H_{\rm th}(0) = 68.9013\,\mathrm{km\,s^{-1}\,Mpc^{-1}}$. The quadratic curve in Figure 1 is plotted using this normalization.

Table 1. Best-fit parameters obtained from the 32 Cosmic Chronometer measurements for the three scale-factor parameterizations using the diagonal-error $\chi^2_{\rm CC}$ defined in the text. Here, H_0 is in km s^{-1} Mpc^{-1} and $p = \psi t_0$ is dimensionless; non-diagonal systematic covariance is not included. The quadratic row reports the corrected minimum obtained by global search followed by local refinement.

Model	H_0	p	n	$\chi^2_{\rm CC}$	dof	$\chi^2_{\rm red}$
Hybrid	69.5781	0.4460	0.4713	11.8497	29	0.4086
Linear	66.1944	0.8156	0.4446	12.3588	29	0.4262
Quadratic	68.9013	0.4891	0.4521	11.9157	29	0.4109

3.4. Statistical Model Comparison

To compare the three scale-factor prescriptions with the flat ΛCDM model, we use the reduced chi-square, Akaike Information Criterion (AIC), and Bayesian Information Criterion (BIC). For $N = 32$ measurements, these quantities are defined using the number k of fitted parameters ($k = 3$ for each kinematic prescription and $k = 2$ for flat ΛCDM) as

$$\chi^2_{\rm red} = \frac{\chi^2_{\rm CC}}{N-k}, \qquad \mathrm{AIC} = \chi^2_{\rm CC} + 2k, \qquad \mathrm{BIC} = \chi^2_{\rm CC} + k\ln N. \tag{51}$$

Table 2 reports these values. Because the calculation uses the diagonal chi-square in Equation (50), the comparison does not account for the full covariance. Flat ΛCDM has the lowest AIC and BIC, although the differences from the three kinematic models are modest.

Table 2. Statistical comparison of the three scale-factor prescriptions and flat ΛCDM using the same 32 Cosmic Chronometer measurements and diagonal-error likelihood.

Model	χ^2_{CC}	χ^2_{red}	AIC	ΔAIC	BIC	ΔBIC
Flat ΛCDM	11.6554	0.3885	15.6554	0.0000	18.5887	0.0000
Hybrid	11.8497	0.4086	17.8497	2.1943	22.2469	3.6582
Linear	12.3588	0.4262	18.3588	2.7034	22.7560	4.1673
Quadratic	11.9157	0.4109	17.9157	2.2603	22.3129	3.7242

Table 2 shows that the flat ΛCDM model gives the lowest AIC and BIC values for the present CC data. However, the differences between this model and the three scale-factor models are not very large. Thus, the three prescribed histories also provide comparable fits to the CC data. The present analysis uses diagonal errors and does not include the full systematic covariance of the CC measurements, so the model ranking should be read with this limitation in mind.

3.5. CC-Constrained Reconstruction of the EoS

For Figure 3, we use the best-fit values of H_0, $p = \psi t_0$, and n obtained from the 32 CC measurements (Table 1); these parameters are not refitted for the figure. We calculate $H(t)$ and its derivatives from Equations (19)–(37), relate redshift to time through $a(t)/a(t_0) = (1+z)^{-1}$, and obtain the total effective density and EoS from Equations (12) and (17). We keep $c = 1.2$, Ω_{m0}, and α/H_0 fixed and vary Δ over the presented range. The surfaces illustrate how the reconstructed EoS changes with Δ for each history.

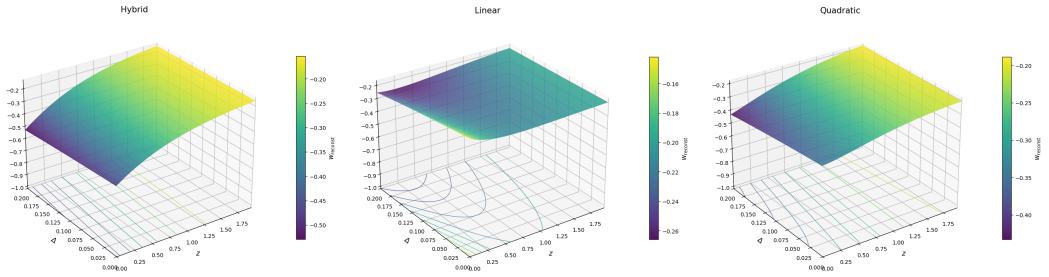
The parameter-setting procedure adopted for Figure 3 can be summarized as

$$\underbrace{(H_0, p, n)}_{\text{CC constrained}}, \qquad \underbrace{\left(c, \frac{\alpha}{H_0}, \Omega_{m0}\right)}_{\text{fixed independently}}, \qquad \underbrace{\Delta}_{\text{varied}}, \tag{52}$$

where the first set is determined from the CC analysis, the second is fixed independently, and only Δ is varied to examine the sensitivity of the reconstructed EoS. The holographic contribution is controlled by the dimensionless parameter c. Since c is not constrained by the CC-only background reconstruction, we adopt $c = 1.2$ as a fiducial value. Ref. [69] constrains the coefficients of the standard event-horizon holographic and Ricci dark-energy models separately. It reports tensions between data combinations, including poor viability of the standard Ricci model once early-universe information is included. Those constraints do not transfer directly to the dimensionally different Barrow–Ricci density used here. The value $c = 1.2$ is therefore a fiducial choice only, and c and α are not constrained by the CC-only analysis. This value is held fixed during the reconstruction so that we can study the effect of the Barrow deformation parameter Δ without an additional degeneracy due to c.

Figure 3 shows how the reconstructed EoS varies with Δ for the three scale-factor histories.

While concluding the current section, it is important to emphasize that the reconstructed equation of state parameter w_{reconst} derived in this framework represents the total effective fluid of the universe (combining both dark-energy and pressureless-matter components) rather than the dark-energy sector only. Consequently, direct comparisons between w_{reconst} and observational bounds restricted strictly to dark energy (such as $w = -1$ quintessence/phantom boundaries) must be interpreted taking the combined-fluid contribution into consideration.



(**a**) Hybrid model. (**b**) Linear model. (**c**) Quadratic model.

Figure 3. Three-dimensional sensitivity of the CC-constrained reconstructed total-fluid EoS parameter $w_{\rm tot} \equiv w_{\rm reconst}$ to redshift z and the Barrow deformation parameter Δ for the hybrid, linear, and quadratic scale-factor models. The plotted quantity includes pressureless matter and is not the dark-energy-only EoS. The CC-constrained background parameters (H_0, p, n) are kept fixed, while the remaining parameters are fixed at the values specified in the text. The variation of the surface with $0 \leq \Delta \leq 0.2$ illustrates the dependence of the reconstructed EoS on the Barrow deformation parameter.

4. Approach II: Reconstructing BHDE as Ghost Dark Energy

In Approach II, the exact correspondence between BHDE and GDE under a Hubble cutoff implies an underlying exponential expansion history ($H = H_0$). The linear and quadratic Taylor expansions implemented here should thus be regarded as phenomenological approximations designed to test deviations near the present epoch rather than exact analytic solutions of the foundational correspondence condition across all redshifts. In the following subsections we elaborate the detailed methodology.

4.1. BHDE–GDE Correspondence

In this subsection, we impose the correspondence $\rho_{\rm BHDE} = \rho_{\rm GDE}$. The purpose is to test whether the Barrow entropy-corrected holographic component can reproduce the background scaling of QCD ghost dark energy without treating GDE as a separate component. The correspondence defines a single effective dark-energy sector and tests the relation between the two constructions.

BHDE–GDE Correspondence Under Hubble Infrared Cutoff

We choose the Hubble horizon as the infrared (IR) cutoff:

$$L = \frac{1}{H}. \tag{53}$$

With $L = 1/H$, the holographic dark-energy density is directly related to the Hubble parameter, which simplifies the correspondence analysis.

In Approach II, we impose the correspondence

$$\rho_{BHDE} = \rho_{GDE}. \tag{54}$$

Under this assumption, using the general expression of BHDE density, we obtain

$$3c^2 L^{\Delta-2} = \alpha H. \tag{55}$$

Setting $L = 1/H$ gives an algebraic relation between the Hubble parameter and the model parameters.

Solving this relation, we obtain

$$H = \frac{\dot{a}}{a} = \left(\frac{\alpha}{3c^2}\right)^{\frac{1}{1-\Delta}} = H_0, \tag{56}$$

where a denotes the scale factor. Thus, the exact correspondence gives a constant Hubble rate and hence an exponential solution. The linear and quadratic scale factors introduced below are Taylor truncations of this exponential form; they are not independent exact solutions of Equation (56). The truncations are used to test the sensitivity of the reconstructed EoS to the order of the scale-factor expansion.

Integrating gives the scale factor

$$a(t) = a_0 e^{H_0 t}. \tag{57}$$

The dark-energy density is then

$$\rho_{DE} = 3c^2 H^{2-\Delta} = 3c^2 \left(\frac{\alpha}{3c^2}\right)^{\frac{2-\Delta}{1-\Delta}}. \tag{58}$$

The total effective energy density, including matter, is

$$\rho_{eff} = 3c^2 \left(\frac{\alpha}{3c^2}\right)^{\frac{2-\Delta}{1-\Delta}} + \rho_{m0} a^{-3}. \tag{59}$$

Here, the first term represents the constant dark-energy contribution, while the second term corresponds to the pressureless-matter component, which decreases with the expansion of the universe.

Using $a(t) = a_0 e^{H_0 t}$, the effective density explicitly becomes

$$\rho_{eff} = 3c^2 \left(\frac{\alpha}{3c^2}\right)^{\frac{2-\Delta}{1-\Delta}} + \rho_{m0} \left(a_0 e^{H_0 t}\right)^{-3}. \tag{60}$$

Differentiating Equation (60) gives the time derivative of the effective energy density:

$$\dot{\rho}_{\text{eff}} = -\frac{3H_0 \rho_{m0}}{a_0^3} e^{-3H_0 t}. \tag{61}$$

Substituting the effective density and its time derivative from Equations (60) and (61) into Equation (16), we obtain the reconstructed EoS in Approach II:

$$w_{reconst,ApproachII} = -1 + \frac{H_0 \rho_{m0}}{H\left(3^{\frac{1}{\Delta-1}} a_0^3 e^{3H_0 t} \alpha \left(\frac{\alpha}{c^2}\right)^{\frac{1}{1-\Delta}} + \rho_{m0}\right)}. \tag{62}$$

From Equation (62), we see that the deviation of the total-fluid EoS parameter $w_{\text{tot}} = w_{\text{reconst}}$ from -1 depends on the matter density ρ_{m0} and the exponential term $e^{3H_0 t}$. As $z \to \infty$, the dust density becomes dominant and w_{tot} approaches zero. However, this does not mean that the universe passes through a matter-dominated phase because $H = H_0$ remains constant in this model. This happens because, in the present approach, the Friedmann equation is not imposed on the dust density together with the constant dark-energy density. At the present time ($t = 0$), the value of w_{tot} is greater than -1. This value describes the combined fluid and should not be taken as the EoS of dark energy alone. Since the dark-energy density is assumed to be constant, its EoS is $w_{\text{DE}} = -1$ if the dark-energy component is separately conserved. Therefore, in this exact correspondence, the de Sitter

expansion follows from the constant value of H and not simply from the limiting value of the total-fluid EoS.

Figure 4 presents the reconstructed total-fluid equation-of-state parameter $w_{\rm tot}(z) \equiv w_{\rm reconst}(z)$ for the BHDE–GDE correspondence in Approach II. It includes the pressureless-matter contribution and must not be interpreted as the dark-energy-only EoS. In this case, the correspondence condition with the Hubble horizon cutoff fixes the Hubble rate to the constant value $H = H_0$, leading to the exponential scale factor $a(t) = a_0 e^{H_0 t}$ given in Equation (57). Using the standard redshift definition $1 + z = a_0/a(t)$ gives

$$t(z) = -\frac{\ln(1+z)}{H_0}. \tag{63}$$

The exponential factors in the density and its time derivative are $e^{-3H_0 t} = (1+z)^3$ and $e^{3H_0 t} = (1+z)^{-3}$. Substituting these expressions into Equation (62) gives the EoS as a function of redshift. We plot it over $-0.5 \leq z \leq 2$, covering the recent past and a moderate future interval without approaching $z = -1$. We set $H_0 = 1$, $c = 1.2$, and $\Omega_{m0} = 0.30$ and use $\Delta = 0.10$, 0.15, and 0.20. The CC fit in Section 3 does not constrain the pure exponential background, so $H_0 = 1$ is a normalization choice. The correspondence fixes $\alpha / H_0^{1-\Delta} = 3c^2 = 4.32$.

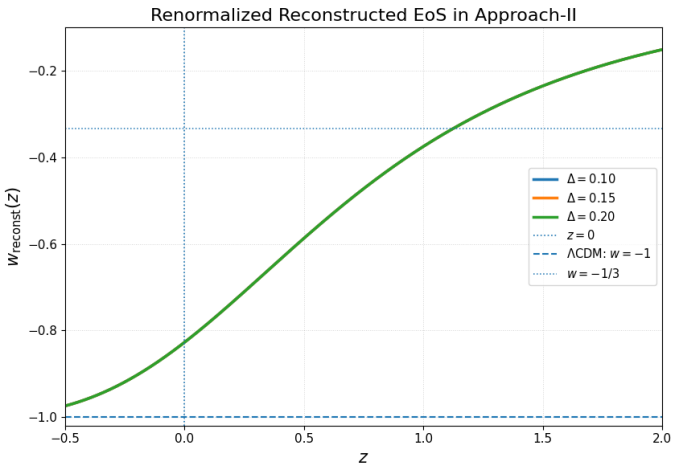


Figure 4. Redshift evolution of the reconstructed total-fluid equation-of-state parameter $w_{\rm tot}(z) \equiv w_{\rm reconst}(z)$, including pressureless matter and the effective dark-energy sector, for the hybrid BHDE–GDE correspondence. The curves correspond to $\Delta = 0.10$, 0.15, and 0.20. The vertical dotted line marks $z = 0$; the horizontal lines mark $w_{\rm tot} = -1$ and $w_{\rm tot} = -1/3$ for reference only. The curves use the common dimensionless convention $H_0 = 1$, $c = 1.2$, and $\Omega_{m0} = 0.30$. The plotted $w_{\rm tot}$ is not the dark-energy-only EoS.

The three curves in Figure 4 nearly overlap. At the present epoch, $w_{\rm reconst}(0) \simeq -0.8276$ describes the combined dark-energy-plus-matter fluid, not dark energy alone. For the exact BHDE–GDE correspondence, the dark-energy density is constant and $w_{\rm DE} = -1$; the total-fluid value should therefore not be compared directly with DESI constraints on the dark-energy EoS. The weak dependence on Δ arises from the normalization used here: the correspondence fixes $H = H_0$, so $E = H/H_0 = 1$ and the factor $E^{2-\Delta}$ is unity. This is a degeneracy of the adopted prescription, not evidence that the Barrow parameter has no effect in general. The time origins also differ between sections: in Section 3, $t_0 > 0$ is the present cosmic age, whereas here $t = 0$ is the present epoch and $a_0 = a(0)$; thus $t < 0$ refers to the past. The two conventions should not be mixed in the Taylor expansions below.

Reconstructed EoS Parameter in Approach II for Linearly and Quadratically Truncated Scale Factor

Expanding the scale factor in Equation (57), $a(t) = a_0 e^{H_0 t}$, to first order gives

$$a(t)_{linear} \approx a_0(1 + H_0 t) \tag{64}$$

Expanding Equation (57) to second order gives

$$a(t)_{quadratic} \approx a_0\left(1 + H_0 t + \frac{H_0^2 t^2}{2}\right). \tag{65}$$

Scope and consistency of the truncated histories.

The exact BHDE–GDE correspondence in Equation (56) requires constant H for fixed c, α, and $\Delta < 1$. Therefore, the linear and quadratic scale factors are treated below as phenomenological Taylor-truncated histories, not exact solutions of the correspondence condition. Normalizing the densities to agree at $H = H_0$, their ratio for a time-dependent trial history is

$$\frac{\rho_{\mathrm{BHDE}}}{\rho_{\mathrm{GDE}}} = \left(\frac{H}{H_0}\right)^{1-\Delta}.$$

For the linear history, we have $H/H_0 = 1 + z$, whereas, for the quadratic history, $H/H_0 = \sqrt{1 - z^2}$ within the real-valued redshift range. Thus, both densities have the same value at $z = 0$, but their values become different at other redshifts. At $z = 0.95$, the density ratio is found to be 1.82, 1.76, and 1.71 for $\Delta = 0.10$, 0.15, and 0.20, respectively, for the linear case. For the quadratic case, the corresponding values are 0.35, 0.37, and 0.39 (Figure 5b). These values show that the differences are substantial. Thus, rather than treating the linear and quadratic histories as close approximations of the exact solution, we consider them as two distinct phenomenological models. In the following calculations, we keep the constant dark-energy term as a reference density taken from the exact exponential solution. Therefore, the behavior of the EoS parameter obtained here depends on this choice and should not be considered as exact results of the BHDE–GDE correspondence.

For the linearly truncated scale factor (64), the Hubble parameter and its first time derivative are

$$H(t) = \frac{H_0}{1 + H_0 t}, \tag{66}$$

and

$$\dot{H}(t) = -\frac{H_0^2}{(1 + H_0 t)^2} \tag{67}$$

respectively.

Also, the Hubble parameter and its first time derivative for quadratically truncated scale factor (65) are

$$H(t) = \frac{2H_0(1 + H_0 t)}{2 + H_0 t(2 + H_0 t)}, \tag{68}$$

and

$$\dot{H}(t) = -\frac{2H_0^3 t(2 + H_0 t)}{[2 + H_0 t(2 + H_0 t)]^2} \tag{69}$$

respectively.

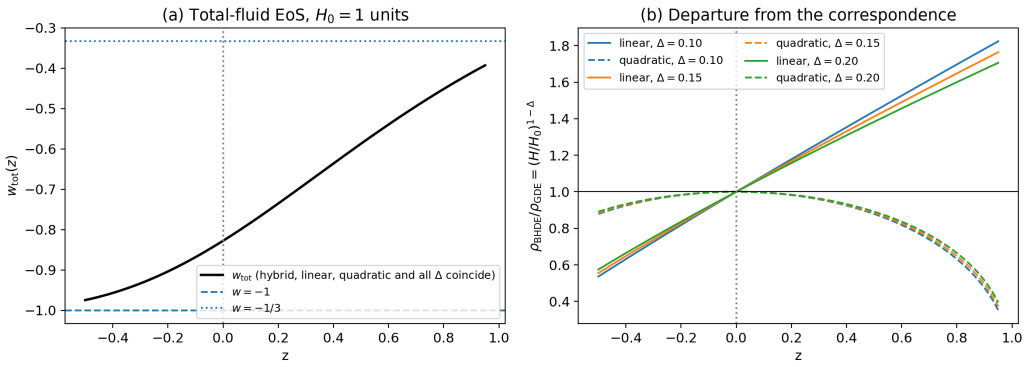


Figure 5. (**a**) Reconstructed total-fluid EoS $w_{\rm tot}(z) \equiv w_{\rm reconst}(z)$ in Approach II in the common dimensionless convention ($H_0 = 1$, $c = 1.2$, $\Omega_{m0} = 0.30$); the exponential, linearly truncated and quadratically truncated histories and all $\Delta = 0.10, 0.15, 0.20$ give the same curve. The horizontal lines $w = -1$ and $w = -1/3$ are reference levels only, and the plotted quantity includes pressureless matter and is not the dark-energy-only EoS. (**b**) Density ratio $\rho_{\rm BHDE}/\rho_{\rm GDE} = (H/H_0)^{1-\Delta}$ for the linear (solid) and quadratic (dashed) truncations, which measures the departure of the truncated histories from the exact correspondence $\rho_{\rm BHDE} = \rho_{\rm GDE}$.

Thus, for linearly truncated scale factor (64), the effective density is given by

$$\rho_{eff,linear} = 3c^2 H_0^{2-\Delta} + \rho_{m0}[a_0(1 + H_0 t)]^{-3}, \tag{70}$$

and, for quadratically truncated scale factor (65), the effective density is given by

$$\rho_{eff,quadratic} = 3c^2 H_0^{2-\Delta} + \rho_{m0}\left[a_0\left(1 + H_0 t + \frac{H_0^2 t^2}{2}\right)\right]^{-3} \tag{71}$$

Differentiating Equations (70) and (71) gives the density derivatives for the linear and quadratic histories

$$\dot{\rho}_{\rm eff,linear} = -\frac{3H_0\rho_{m0}}{a_0^3(1 + H_0 t)^4} \tag{72}$$

and

$$\dot{\rho}_{\rm eff,quadratic} = -\frac{48H_0(1 + H_0 t)\rho_{m0}}{a_0^3(2 + H_0 t(2 + H_0 t))^4} \tag{73}$$

respectively.

Substituting the expressions of effective energy densities, given by Equations (70) and (71), and their respective time derivatives, given by Equations (72) and (73), into Equation (16), the effective reconstructed EoS parameters for linearly and quadratically truncated scale factors are

$$w_{reconst,ApproachII,linear} = -1 + \frac{H_0^{1+\Delta}\rho_{m0}}{3a_0^3c^2HH_0^2(1 + H_0 t)^4 + HH_0^{\Delta}(1 + H_0 t)\rho_{m0}} \tag{74}$$

and

$$w_{reconst,ApproachII,quadratic} = -1 + \frac{16H_0^{1+\Delta}(1 + H_0 t)\rho_{m0}}{H(2 + H_0 t(2 + H_0 t))\left[3a_0^3c^2H_0^2(2 + H_0 t(2 + H_0 t))^3 + 8H_0^{\Delta}\rho_{m0}\right]} \tag{75}$$

respectively.

In the common dimensionless convention ($H_0 = 1$, $\bar{\rho}_{\rm DE} = 3c^2 = 4.32$, $\bar{\rho}_{m0} = 3\Omega_{m0} = 0.90$) the factors H_0^{Δ} in Equations (74) and (75) equal unity, and the Hubble rate cancels in $\dot{\rho}_{\rm eff}/(3H\rho_{\rm eff})$. With $a(t)/a_0 = (1 + z)^{-1}$ every history then gives the same function,

$w_{\rm tot}(z) = -1 + \bar{\rho}_m/(\bar{\rho}_{\rm DE} + \bar{\rho}_m) = -1 + 0.9(1+z)^3/[4.32 + 0.9(1+z)^3]$, independent of Δ and the truncation order. Any Δ dependence of the linear and quadratic results that were obtained by inserting a numerical H_0 in km s^{-1} Mpc^{-1} into $H_0^{-\Delta}$ is a unit artifact and is not retained. (The constant $\bar{\rho}_{\rm DE}$ is a reference value; Friedmann closure $3 = \bar{\rho}_{\rm DE} + \bar{\rho}_{m0}$ is not imposed on this sector for $c = 1.2$).

In Table 3, the values in the first three columns are for the total fluid, including pressureless matter. Therefore, these values should not be taken as the EoS of dark energy alone or directly compared with the observational constraints on dark energy. In all three histories considered here, the non-matter part is taken as the constant density $\rho_{\rm DE} = 3c^2 H_0^{2-\Delta}$. If this component is conserved separately, we get $w_{\rm DE} = -1$ from its continuity equation. For the truncations leading to linear and quadratic histories also, this result comes from the assumption of constant dark-energy density. It does not imply that these two histories satisfy the exact BHDE–GDE correspondence. Therefore, we do not compare the total-fluid values in the first three columns with the DESI constraint on dark energy.

Table 3. Present-day total-fluid EoS values $w_{\rm tot}(0) = w_{\rm reconst}(z = 0)$ for the hybrid, linear, and quadratic scale-factor prescriptions. The final column reports $w_{\rm DE,0}$ under the constant dark-energy-density prescription used in the corresponding effective-density expressions. For the truncated histories, this is a consequence of the adopted density ansatz and is not an independent test of the exact BHDE–GDE correspondence. All values use the common dimensionless convention $H_0 = 1$ with $c = 1.2$ and $\Omega_{m0} = 0.30$.

Δ	$w_{\rm tot,0}^{\rm hybrid}$	$w_{\rm tot,0}^{\rm linear}$	$w_{\rm tot,0}^{\rm quadratic}$	$w_{\rm DE,0}$ **(Constant-Density Ansatz)**
0.10	−0.8276	−0.8276	−0.8276	−1
0.15	−0.8276	−0.8276	−0.8276	−1
0.20	−0.8276	−0.8276	−0.8276	−1

We first employ the scale factors truncated linearly and quadratically through Equation (64) and Equation (65), respectively. Their corresponding Hubble parameters and first time derivatives are given by Equations (66)–(69), while the effective densities and their time derivatives follow from Equations (70)–(73). Substitution into the effective-fluid relation, Equation (16), yields the reconstructed EoS expressions in Equations (74) and (75).

The conversion from cosmic time to redshift is performed from $a(t)/a(t_0) = (1+z)^{-1}$. For the linear truncation this gives

$$H_0 t = -\frac{z}{1+z}, \tag{76}$$

whereas, for the quadratic truncation, one obtains

$$H_0 t = -1 + \sqrt{\frac{1-z}{1+z}}. \tag{77}$$

The latter relation restricts the real-valued reconstruction to $z \leq 1$; accordingly, Figure 5 is displayed over a common range $-0.5 \leq z \leq 0.95$. The coefficient α is fixed through $\alpha/H_0^{1-\Delta} = 3c^2 = 4.32$, and the evaluation uses the common dimensionless convention described above ($H_0 = 1$, $c = 1.2$, $\Omega_{m0} = 0.30$) for $\Delta = 0.10$, 0.15 and 0.20. The H_0 values of the Section 3 fits are not used here because the fitted (p, n) do not constrain these pure polynomial histories.

Figure 5a shows the total-fluid EoS implied by the two truncation schemes. In the common convention it is the same function of z for both truncations and for all Δ (see above): $w_{\rm tot} = -0.7353$, -0.5872 and -0.4515 at $z = 0.2$, 0.5 and 0.8. These values are

reported as total-fluid diagnostics only. The truncation order and Δ enter only through the density ratio in Figure 5b, not through $w_{\rm tot}$.

At $z = 0$, Table 3 lists $w_{\rm tot,0} = -0.8276$ for all three histories and all Δ. These values describe the combined fluid and are not dark-energy EoS estimates; they are therefore not classified as quintessence-like dark-energy values or compared with the DESI dark-energy constraint. Under the constant non-matter density explicitly adopted in Equations (70) and (71), the corresponding dark-energy EoS is $w_{\rm DE} = -1$ if that component is separately conserved. For the truncated backgrounds this is a property of the adopted density prescription, not a demonstration that the histories satisfy the exact constant-H correspondence.

5. Reconstruction of the Deceleration Parameter q

The deceleration parameter characterizes the expansion dynamics and the transition between decelerated and accelerated phases [60,70]. Within the homogeneous and isotropic Friedmann–Lemaître–Robertson–Walker (FLRW) framework, it is defined as $q = -\frac{a\ddot{a}}{\dot{a}^2}$, where $a(t)$ denotes the cosmic scale factor [59,60]. Observational evidence from Type Ia supernovae, cosmic microwave background radiation, and baryon acoustic oscillations strongly supports the existence of a late-time accelerated expansion, implying that the present value of the deceleration parameter is negative [1–4].

The deceleration parameter is mathematically expressed in terms of the Hubble parameter as

$$q_{reconst} = -1 - \frac{\dot{H}}{H^2}, \tag{78}$$

which relates cosmic acceleration directly to the time evolution of the Hubble rate [70]. This form is useful here because the expansion history is specified through $H(t)$. Positive values of q correspond to deceleration, whereas negative values indicate accelerated expansion [8,9]. The evolution of q therefore shows whether a prescribed history passes from deceleration to late-time acceleration.

Substituting the three Hubble functions and their first time derivatives into Equation (78) gives the corresponding deceleration parameters:

$$q_{\rm reconst,case1}(t) = -1 + \frac{n}{(n+\psi t)^2} \tag{79}$$

$$q_{\rm reconst,case2}(t) = -1 + \frac{n + 2n\psi t + (n+1)\psi^2 t^2}{[n + (n+1)\psi t]^2} \tag{80}$$

$$q_{\rm reconst,3}(t) = -1 + \frac{n\left(1 + \psi t + \frac{\psi^2 t^2}{2}\right)^2 + \psi^3 t^3 \left(1 + \frac{\psi t}{2}\right)}{\left[n\left(1 + \psi t + \frac{\psi^2 t^2}{2}\right) + \psi t(1+\psi t)\right]^2}. \tag{81}$$

To compare the reconstructed deceleration parameters with the redshift evolution, we introduce the dimensionless time $x = t/t_0$ and use the CC-constrained parameter $p = \psi t_0$. The relation $a(t)/a(t_0) = (1+z)^{-1}$ then determines $x(z)$ numerically for each scale-factor prescription. Substitution into Equations (79)–(81) gives the corresponding $q_{\rm reconst}(z)$ curves. Because the calculation uses $x = t/t_0$, the explicit dependence on H_0 cancels.

Figure 6 shows the redshift z evolution of the reconstructed deceleration parameter q for the hybrid, linear-truncation and quadratic-truncation scale-factor prescriptions. In all three cases the qualitative behavior is similar: q is negative at the present epoch, indicating accelerated expansion, and becomes positive toward higher redshifts, corresponding to a

decelerated expansion phase. Thus all three reconstructed backgrounds show a transition from decelerated to accelerated expansion as the universe evolves to the present epoch.

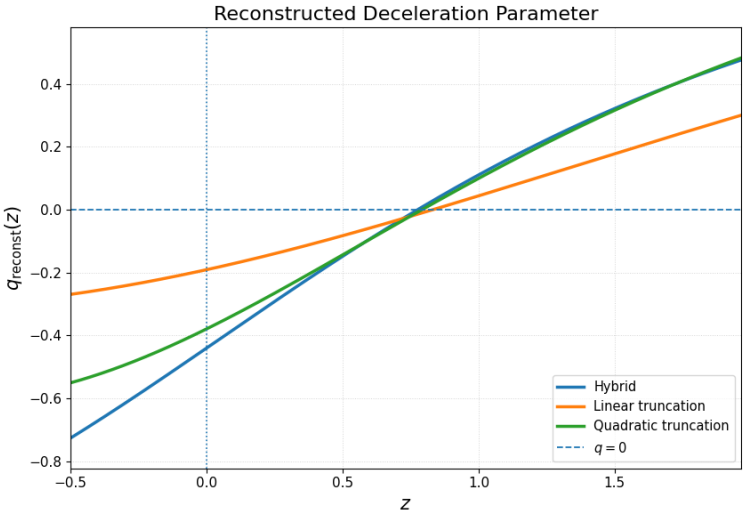


Figure 6. Evolution of the reconstructed deceleration parameter $q_{\mathrm{reconst}}(z)$ with z for the hybrid, linear-truncation, and quadratic-truncation scale factors presented in Equations (79)–(81). The curves are obtained using the corresponding CC-constrained values of p and n listed in Table 1. The horizontal line $q = 0$ divides the accelerated ($q < 0$) and decelerated ($q > 0$) expansion regimes, while the vertical line at $z = 0$ represents the present epoch.

The present values of the deceleration parameter are approximately $q_{\mathrm{reconst}}(0) = -0.4399$, -0.1909 and -0.3791 for the hybrid, linear and quadratic cases, respectively. The corresponding transition from deceleration to acceleration, defined by $q_{\mathrm{reconst}}(z_t) = 0$, occurs at about $z_t \simeq 0.776$, 0.832, and 0.792, respectively. The three histories differ quantitatively but show a similar overall pattern and close transition redshifts. The hybrid and quadratic histories evolve similarly over much of the interval, while the linear history has a less negative present-day value of q_{reconst}.

6. Incorporation of $f(T)$ Gravity

We combine the Barrow–Ricci and QCD ghost terms in the effective energy density and pressure. We then study this effective sector in $f(T)$ gravity. Similar effective-fluid constructions appear in Refs. [71,72].

We now embed the BH–Ricci and QCD ghost dark-energy sectors into the teleparallel modified-gravity framework described by a general function $f(T)$ of the torsion scalar T. The action is taken as [40,73–75]

$$S = \frac{1}{2\kappa^2}\int d^4x\, e\, f(T) + S_m + S_{\mathrm{BH-Ricci}} + S_{\mathrm{GDE}}, \tag{82}$$

where $e = \det(e^A{}_\mu) = \sqrt{-g}$, $\kappa^2 = 8\pi G$, and S_m denotes the matter action. For a spatially flat FLRW background, the torsion scalar is

$$T = -6H^2, \tag{83}$$

where $H = \dot{a}/a$ is the Hubble parameter.

Variation of the action with respect to the tetrad gives the modified Friedmann equations. In the convention $T = -6H^2$, they can be written as

$$\kappa^2 \rho_{\rm src} = \frac{1}{2}\Big(f + 12H^2 f_T\Big), \tag{84}$$

$$\kappa^2 p_{\rm src} = -\frac{1}{2}\Big[f + 4(3H^2 + \dot{H})f_T - 48H^2\dot{H}f_{TT}\Big], \tag{85}$$

where $f_T \equiv df/dT$ and $f_{TT} \equiv d^2 f/dT^2$. Here $\rho_{\rm src}$ and $p_{\rm src}$ denote the explicit source density and pressure, including matter and the two phenomenological dark-energy components but excluding the effective torsional contribution. This notation is used consistently below.

We isolate the purely geometrical contribution generated by departures from the TEGR form $f(T) = T$. With $M_{\rm Pl}^2 = 1/\kappa^2$, we define the effective torsional density and pressure by subtracting the TEGR terms from the modified Friedmann equations:

$$\rho_T \equiv \frac{M_{\rm Pl}^2}{2}(2Tf_T - f - T), \tag{86}$$

$$p_T \equiv \frac{M_{\rm Pl}^2}{2}\Big[f + 4(3H^2 + \dot{H})f_T - 48H^2\dot{H}f_{TT} - 6H^2 - 4\dot{H}\Big]. \tag{87}$$

These definitions make the decomposition $3M_{\rm Pl}^2 H^2 = \rho_{\rm src} + \rho_T$ consistent with the first modified Friedmann equation, where $\rho_{\rm src}$ excludes the torsional contribution. They also give $\rho_T = p_T = 0$ in the TEGR limit $f(T) = T$, $f_T = 1$, and $f_{TT} = 0$. For $f_{\rm PL}(T) = T + \beta(-T)^m$ with $T = -6H^2$, this convention gives $\rho_T^{\rm PL} = M_{\rm Pl}^2\beta(m - 1/2)(6H^2)^m$; the factor is $(m - 1/2)$, not $(1/2 - m)$. The pressure definition follows from the Einstein-form rewriting $-M_{\rm Pl}^2(3H^2 + 2\dot{H}) = p_{\rm src} + p_T$, with $p_{\rm src}$ given by the second field equation above. The subtraction terms are written inside the common factor $M_{\rm Pl}^2/2$ as $-6H^2 - 4\dot{H}$; this makes the TEGR limit $p_T = 0$ explicit. With these definitions, ρ_T and p_T satisfy the continuity equation

$$\dot{\rho}_T + 3H(\rho_T + p_T) = 0. \tag{88}$$

For the power-law form the pressure is

$$p_T^{\rm PL} = -M_{\rm Pl}^2\beta\left(m - \frac{1}{2}\right)(6H^2)^m\left[1 + \frac{2m\dot{H}}{3H^2}\right]. \tag{89}$$

With $M_{\rm Pl}^2 = (8\pi G)^{-1} = 1/\kappa^2$, the first Friedmann equation can consequently be expressed as

$$3M_{\rm Pl}^2 H^2 = \rho_m + \rho_{\rm BH-Ricci} + \rho_{\rm GDE} + \rho_T. \tag{90}$$

The explicit dark-energy densities use the same prescription as the earlier reconstruction. In particular, the logarithmic approximation expands the curvature-dependent factor to first order in Δ while retaining the normalization factor $6^{\Delta/2}$ exactly. On the admissible domain $R > 0$, its dimensionally restored form is

$$\rho_{\rm BH-Ricci} = \frac{c^2}{2}6^{\Delta/2}M_{\rm Pl}^2 R\left[1 - \frac{\Delta}{2}\ln\left(\frac{R}{H_0^2}\right)\right], \qquad R = 6(\dot{H} + 2H^2), \tag{91}$$

$$\rho_{\rm GDE} = \alpha H. \tag{92}$$

The logarithm therefore acts only on the dimensionless curvature R/H_0^2. All the reconstruction and residual calculations use this same first-order prescription; the unexpanded fractional-power expression is not substituted in later sections.

Effective dark-energy sector and equation of state.

For the background reconstruction, we collect all non-matter contributions into a single effective dark-energy sector,

$$\rho_{\rm DE}^{\rm tot} = \rho_{\rm BH-Ricci} + \rho_{\rm GDE} + \rho_T. \tag{93}$$

Rather than assigning separate phenomenological pressures to the individual BH–Ricci and ghost components, we define the effective pressure of the total non-matter sector through the background continuity equation,

$$p_{\rm DE}^{\rm tot} = -\rho_{\rm DE}^{\rm tot} - \frac{\dot{\rho}_{\rm DE}^{\rm tot}}{3H}. \tag{94}$$

Accordingly, the reconstructed total dark-energy equation-of-state parameter is

$$w_{\rm DE}^{\rm tot} = -1 - \frac{1}{3H}\frac{\dot{\rho}_{\rm DE}^{\rm tot}}{\rho_{\rm DE}^{\rm tot}}. \tag{95}$$

This definition incorporates the Barrow–Ricci, ghost, and torsional contributions into a single effective sector without requiring an independent pressure prescription for each phenomenological component.

Background reconstruction and consistency of the $f(T)$ field equations

In this subsection, we consider the prescribed scale factors as phenomenological backgrounds, from which $H(t)$ and $\dot{H}(t)$ are obtained. Subsequently, we fix the corresponding matter and explicit dark-energy densities by the background reconstruction. The prescription of $a(t)$, the choice of the two dark-energy densities, and the subsequent choice of an $f(T)$ function are not considered here as three independent assumptions. Instead, the first modified Friedmann equation is used to determine the gravitational function that is compatible with the prescribed background.

It is useful to separate the matter and explicit dark-energy sources from the purely geometrical contribution. We therefore define

$$\rho_{\rm src} = \rho_m + \rho_{\rm BH-Ricci} + \rho_{\rm GDE}. \tag{96}$$

For the numerical residual calculation, we use dimensionless quantities relative to the present Hubble scale and write $\bar{R} = R/H_0^2$ and $\bar{\rho}_i = \rho_i/(M_{\rm Pl}^2 H_0^2)$. The matter contribution is $\bar{\rho}_m(z) = 3\Omega_{m0}(1+z)^3$ with $\Omega_{m0} = 0.30$. The BH–Ricci term is evaluated using the first-order expression in Equation (11). The logarithm is applied to the dimensionless curvature $\bar{R}$. The ghost contribution in this numerical convention is $\bar{\rho}_{\rm GDE} = 4.32E$, where $E = H/H_0$ and $4.32 = 3c^2$ for $c = 1.2$. The residuals shown below refer to this adopted dimensionless source prescription; the same convention is used for the three background histories.

Using $T = -6H^2$, the first modified Friedmann equation for the explicit sources becomes

$$2\kappa^2\rho_{\rm src} = f(T) - 2Tf_T. \tag{97}$$

Thus, for a prescribed background, $f(T)$ is determined by the first-order equation

$$2T\frac{df}{dT} - f(T) = -2\kappa^2\rho_{\rm src}(T). \tag{98}$$

For the numerical reconstruction it is convenient to introduce $X = -T = 6H^2 > 0$. Equation (98) then takes the form

$$\frac{df}{dX} - \frac{f}{2X} = -\frac{\kappa^2 \rho_{\rm src}(X)}{X}. \tag{99}$$

Its formal solution is

$$f_{\rm rec}(X) = \sqrt{X}\left[C - \kappa^2 \int^X \frac{\rho_{\rm src}(u)}{u^{3/2}}\, du\right], \tag{100}$$

where the integration constant C is fixed by the chosen present-day normalization. The derivatives f_T and f_{TT} used below are obtained from the reconstructed function. The pressure entering the second background equation is assigned from the continuity equation,

$$p_{\rm src} = -\rho_{\rm src} - \frac{\dot{\rho}_{\rm src}}{3H}. \tag{101}$$

Here $p_{\rm src}$ is the pressure associated with the combined explicit source $\rho_{\rm src} = \rho_m + \rho_{\rm BH-Ricci} + \rho_{\rm GDE}$. Because the matter component is pressureless and separately conserved, Equation (101) reduces to the continuity-defined pressure of the combined BH–Ricci and ghost sector. It is distinct from $p_{\rm DE}^{\rm tot}$ in Equation (95), which also includes the torsional density ρ_T in the effective non-matter sector. The pressure is not fitted independently; it is assigned through the continuity relation in Equation (101). Since the reconstructed function is obtained from the first Friedmann equation and the pressure is defined through background conservation, the second equation is related to the first by the conservation identity subject to the adopted matter-conservation assumptions. We therefore interpret $\mathcal{E}_1$ and $\mathcal{E}_2$ as numerical consistency diagnostics of the implemented reconstruction rather than two wholly independent physical tests. The second residual below is formed directly from the second modified Friedmann equation, including its overall minus sign and the factor $1/2$ multiplying the full bracket. In the first residual, the equivalent forms shown explicitly below follow from $T = -6H^2$ and Equation (97); this makes the factor of two in the first Friedmann equation unambiguous. To quantify the numerical satisfaction of the two equations, we define the normalized residuals

$$\mathcal{E}_1(z) = \frac{f_{\rm rec} - 2T f_{{\rm rec},T} - 2\kappa^2 \rho_{\rm src}}{2\kappa^2 \rho_{\rm src}} = \frac{\frac{1}{2}\left[f_{\rm rec} + 12H^2 f_{{\rm rec},T}\right] - \kappa^2 \rho_{\rm src}}{\kappa^2 \rho_{\rm src}}, \tag{102}$$

and

$$\mathcal{E}_2(z) = \frac{-\frac{1}{2}\left[f_{\rm rec} + 4(3H^2 + \dot{H}) f_{{\rm rec},T} - 48H^2 \dot{H} f_{{\rm rec},TT}\right] - \kappa^2 p_{\rm src}}{\kappa^2 \rho_{\rm src}}. \tag{103}$$

We calculate the residuals in the redshift range $-0.8 \le z \le 2.5$. For each background and $\Delta = 0.10, 0.15, 0.20$, we first calculate $E(z)$ and $\dot{H}/H_0^2$. Then we calculate the final dimensionless source density and obtain $f_{\rm rec}(T)$ by numerical integration of the first-order reconstruction equation. We use cubic spline interpolation for the reconstructed function and its derivatives required in Equations (98) and (99). The pressure is calculated from the continuity equation using the derivative of the same interpolated source density with respect to $X = -T = 6E^2$. After this, both residuals are calculated at each grid point. Their maximum absolute values over the full redshift range and the three values of Δ are given in Table 4. The second residual is mainly a numerical consistency check because the pressure is obtained from the continuity equation. Hence it is not an independent physical test.

Table 4. Maximum absolute residuals of both reconstructed field equations and the power-law ansatz over $-0.8 \leq z \leq 2.5$ together with the minimum value of $f_{\mathrm{PL},T}$. All values use the final dimensionless source-density prescription stated in the text.

Background	$\max\lvert\mathcal{E}_1^{\mathrm{rec}}\rvert$	$\max\lvert\mathcal{E}_2^{\mathrm{rec}}\rvert$	$\max\lvert\mathcal{E}_1^{\mathrm{PL}}\rvert$	$\max\lvert\mathcal{E}_2^{\mathrm{PL}}\rvert$	$\min f_{\mathrm{PL},T}$
Hybrid	7.65×10^{-9}	1.58×10^{-10}	2.20×10^{-1}	2.27×10^{-1}	-3.504
Linear truncation	1.58×10^{-9}	7.19×10^{-10}	9.31×10^{-1}	8.96×10^{-1}	-9.778
Quadratic truncation	8.28×10^{-9}	3.47×10^{-9}	5.32×10^{-1}	5.55×10^{-1}	-5.538

Figure 7 displays the first reconstructed residual. The second reconstructed residual is also evaluated over the same grid and is included in Table 4; an additional plot is omitted for brevity. The reconstructed residuals are small under the numerical procedure and source-density convention stated above. The power-law ansatz is assessed separately below.

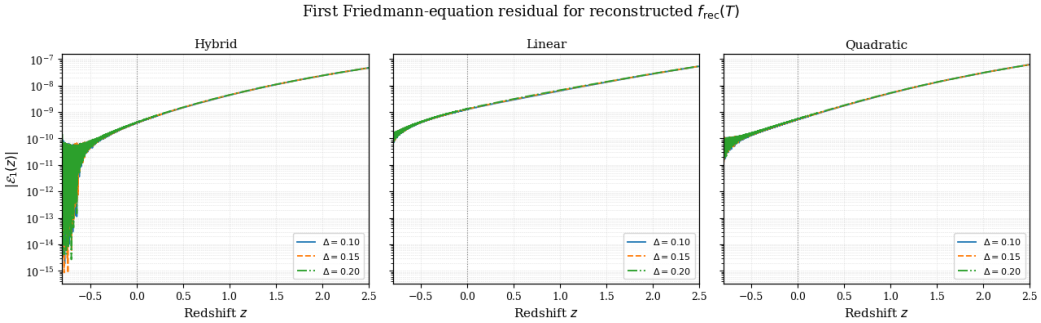


Figure 7. Redshift evolution of the absolute first Friedmann equation residual, $|\mathcal{E}_1(z)|$, for the reconstructed $f_{\mathrm{rec}}(T)$ model over $-0.8 \leq z \leq 2.5$. The panels show the hybrid, linear, and quadratic background histories. The curves correspond to $\Delta = 0.10$, 0.15, and 0.20. The vertical dotted line marks the present epoch, $z = 0$. The maximum absolute values are listed in Table 4.

Power-Law Form of $f(T)$

For comparison with the reconstructed gravitational function, we also consider the commonly used power-law form

$$f_{\mathrm{PL}}(T) = T + \beta(-T)^m. \tag{104}$$

Here β and m define a separate phenomenological power-law ansatz used to compare against the reconstructed function; they are not assumed to provide a parametric representation of $f_{\mathrm{rec}}(T)$ and do not determine the background independently. For $\beta = 0$, the TEGR/GR form is recovered, while the limit $m \to 0$ gives a constant correction at the background level. For Equation (104),

$$f_{\mathrm{PL},T} = 1 - \beta m(-T)^{m-1}, \qquad f_{\mathrm{PL},TT} = \beta m(m-1)(-T)^{m-2}. \tag{105}$$

For this form, the effective torsional density following from Equation (86) is

$$\rho_T^{\mathrm{PL}} = M_{\mathrm{Pl}}^2 \beta \left(m - \frac{1}{2} \right) (6H^2)^m. \tag{106}$$

The sign in Equation (106) follows from the effective-fluid definition in Equation (86) with the torsion convention $T = -6H^2$. This algebraic result does not establish that the power-law ansatz satisfies both modified Friedmann equations; that question is assessed

separately using the normalized residuals in Equations (108) and (109). The background-level viability condition is

$$f_{\mathrm{PL},T}(z) = 1 - \beta m[6H^2(z)]^{m-1} > 0 \quad \text{for every } z \text{ in the analyzed interval.} \tag{107}$$

This inequality must be checked numerically for each scale-factor history and parameter set; it is not assumed to hold merely because β is normalized at $z = 0$. It is a background viability condition, not a complete perturbative stability criterion. To test the power-law form independently, we evaluate the residuals using f_{PL} rather than f_{rec}:

$$\mathcal{E}_1^{\mathrm{PL}}(z) = \frac{\frac{1}{2}[f_{\mathrm{PL}} + 12H^2 f_{\mathrm{PL},T}] - \kappa^2\rho_{\mathrm{src}}}{\kappa^2\rho_{\mathrm{src}}}, \tag{108}$$

$$\mathcal{E}_2^{\mathrm{PL}}(z) = \frac{-\frac{1}{2}[f_{\mathrm{PL}} + 4(3H^2 + \dot{H})f_{\mathrm{PL},T} - 48H^2\dot{H}f_{\mathrm{PL},TT}] - \kappa^2 p_{\mathrm{src}}}{\kappa^2\rho_{\mathrm{src}}}. \tag{109}$$

A normalization at $z = 0$ alone does not establish compatibility at other redshifts. We evaluated Equations (108) and (109) for $m = 0.32$ with β fixed by the first Friedmann equation at $z = 0$. The residuals are appreciable over the analyzed interval. Their maximum absolute values are approximately $(0.220, 0.227)$ for the hybrid background, $(0.931, 0.896)$ for the linear background, and $(0.532, 0.555)$ for the quadratic background. The power-law residual profiles are shown in Figure 8; Table 4 summarizes these results and the minimum value of $f_{\mathrm{PL},T}$. A zero crossing at $z = 0$ in some panels follows from the imposed normalization and does not show consistency at other redshifts. The minimum value of $f_{\mathrm{PL},T}$ is negative for all three backgrounds, so this ansatz additionally fails the background condition in Equation (107). These conclusions apply to the source-density and normalization convention used in this calculation. The numerical values should not be taken as independent constraints on the underlying theory until the dimensional normalization of all source terms is fixed consistently.

Figure 7 shows the absolute first-equation residual for the reconstructed function. Table 4 reports the maximum absolute residuals of both reconstructed field equations, the two residuals for the power-law ansatz, and the minimum value of $f_{\mathrm{PL},T}$.

The background evolution for the hybrid, linear-truncation, and quadratic-truncation scale factors is determined by the corresponding Hubble functions given in Equations (19), (28) and (37) together with their CC-constrained parameter combinations. To maintain consistency with the reconstruction in Sections 3–5, the model-specific values of H_0, $p = \psi t_0$, and n obtained from the cosmic-chronometer analysis are retained for the three scale-factor prescriptions; they are not replaced by a common set of ψ and n values. It is convenient to introduce $x = t/t_0$ so that $\psi t = px$. Thus the conversion from the CC-constrained background to redshift is performed through $\frac{a(t)}{a(t_0)} = \frac{1}{1+z}$, with the appropriate scale factor used separately for each parameterization. No additional arbitrary normalization of ψ or n is introduced in this procedure.

Following a kinematic reconstruction approach, the scale factors and associated Hubble histories are prescribed to evaluate the geometrical and thermodynamic properties of the model. Because the underlying modified field equations are not solved dynamically from the beginning, nonzero residuals appear in the higher-order Friedmann equations. As demonstrated by the power-law ansatz $f_{\mathrm{PL}}(T)$, these residuals highlight the inherent tension between purely kinematic parameterization and the full dynamical constraints of $f(T, B)$ gravity.

For each scale-factor prescription, the CC-constrained values of H_0, $p = \psi t_0$, and n are retained, and $f_{\rm rec}(T)$ is reconstructed separately. The power-law ansatz is used only as a comparison in the field-equation residual test. The effective-fluid equation of state, stability diagnostic, and horizon-entropy calculation discussed below use the CC-constrained background and the explicitly stated effective-density prescription; they are not calculated from the power-law ansatz.

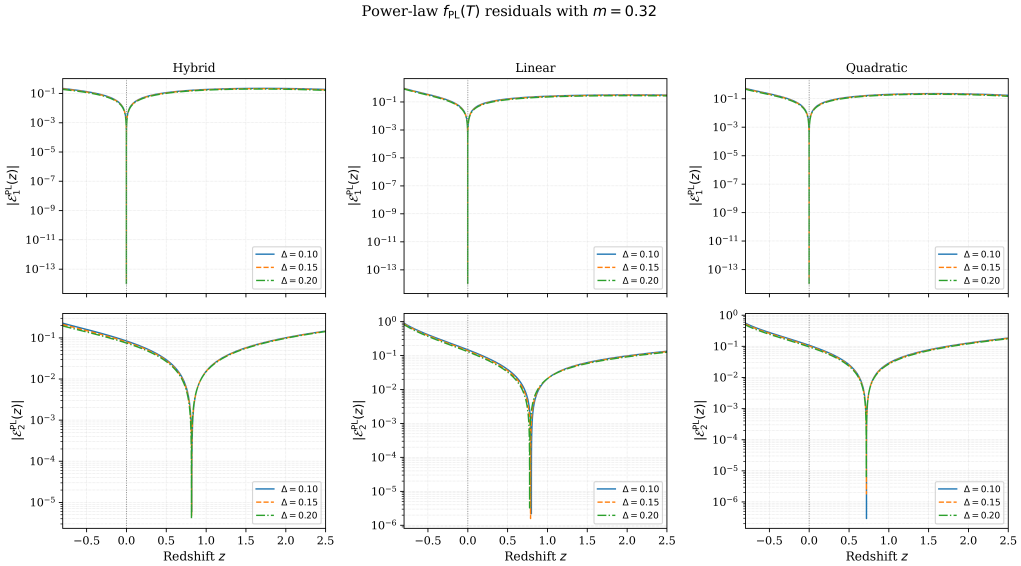


Figure 8. Absolute normalized residuals of the two modified Friedmann equations that were evaluated with the power-law ansatz $f_{\rm PL}(T) = T + \beta(-T)^m$, with $m = 0.32$ and β fixed by the present-day first Friedmann normalization. The columns correspond to the hybrid, linear-truncation, and quadratic-truncation backgrounds; the curves show $\Delta = 0.10$, 0.15, and 0.20. The vertical dotted line marks $z = 0$. Residuals away from zero demonstrate that present-day normalization alone does not make the power-law ansatz consistent with the prescribed backgrounds.

Figure 9 presents the geometrical effective equation-of-state parameter calculated directly from each CC-constrained background history. For this diagnostic, the dimensionless total effective density is defined by $\rho_{\rm DE}^{\rm tot}(z) = 3E^2(z) - \rho_m(z)$, where $E(z) = H(z)/H_0$ and $\rho_m(z) = 3\Omega_{m0}(1+z)^3$ with $\Omega_{m0} = 0.30$. The corresponding parameter is evaluated from the effective-fluid continuity relation,

$$w_{\rm DE}^{\rm tot}(z) = -1 + \frac{1+z}{3\rho_{\rm DE}^{\rm tot}(z)}\frac{d\rho_{\rm DE}^{\rm tot}(z)}{dz}. \tag{110}$$

For each background, the normalization gives $E(0) = 1$, $\rho_m(0) = 0.9$, and $\rho_{\rm DE}^{\rm tot}(0) = 2.1$. The horizontal lines mark $w_{\rm DE}^{\rm tot} = -1$ and $-1/3$, and the vertical line marks $z = 0$. The curves compare the effective-fluid behavior of the three prescribed histories. This quantity is calculated from the expansion history and the adopted matter density. It is therefore a geometrical diagnostic rather than an independent test of the reconstructed $f(T)$ field equations. The power-law ansatz is assessed separately through its field-equation residuals.

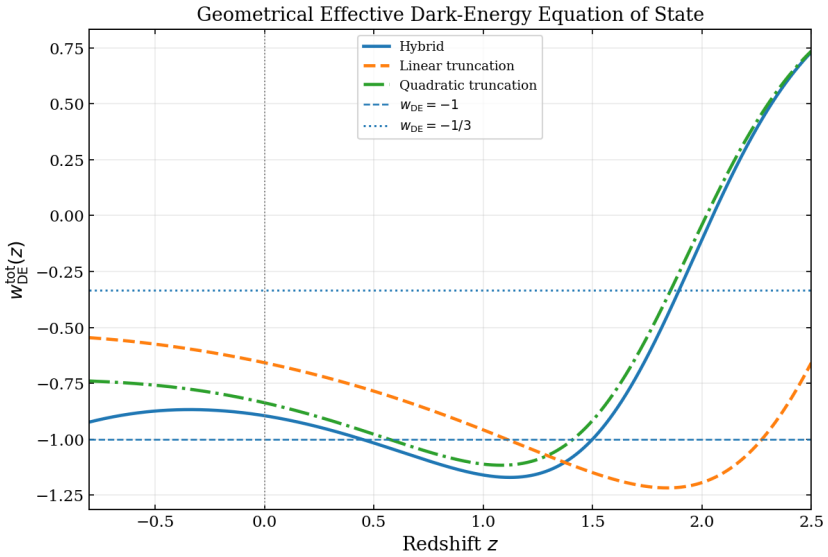


Figure 9. Redshift evolution of the geometrical effective dark-energy equation-of-state parameter, $w_{\rm DE}^{\rm tot}(z)$, for the hybrid, linear-truncation, and quadratic-truncation background models. The effective dark-energy density is defined as $\rho_{\rm DE}^{\rm tot} = 3E^2 - \rho_m$, where $E = H/H_0$ and $\rho_m = 3\Omega_{m0}(1+z)^3$ with $\Omega_{m0} = 0.30$. The horizontal dashed and dotted lines represent $w_{\rm DE}^{\rm tot} = -1$ and $w_{\rm DE}^{\rm tot} = -1/3$, respectively, while the vertical dotted line marks the present epoch, $z = 0$.

7. Stability Analysis Using the Squared Speed of Sound

We use the adiabatic ratio $v_s^2 = \dot{p}/\dot{\rho}$ as a diagnostic of the background effective-fluid description. This quantity is not, by itself, a perturbative stability test of the gravitational degrees of freedom. To avoid mixing two different density prescriptions, we distinguish the Einstein-gravity calculation from the calculation based on the reconstructed $f_{\rm rec}(T)$.

For the Einstein-gravity curves (left column of Figure 10), the non-matter density is the sum of the Barrow–Ricci and QCD ghost terms,

$$\rho_{\rm DE}^{\rm (Ein)} = \rho_{\rm BH-Ricci} + \rho_{\rm GDE}. \tag{111}$$

We use the same first-order Barrow–Ricci prescription as in the reconstruction,

$$\rho_{\rm BH-Ricci} = A_\Delta R\left[1 - \frac{\Delta}{2}\ln\bar{R}\right], \qquad A_\Delta = \frac{c^2}{2}6^{\Delta/2}M_{\rm Pl}^2, \qquad \bar{R} = \frac{R}{H_0^2} > 0, \tag{112}$$

$$\rho_{\rm GDE} = \alpha H, \tag{113}$$

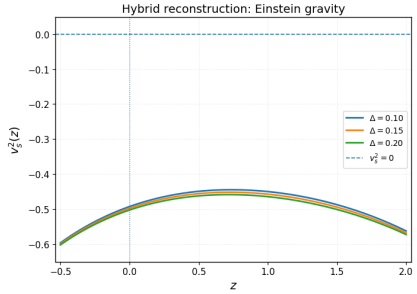
where $R = 6(\dot{H} + 2H^2)$. The corresponding derivatives are

$$\dot{\rho}_{\rm BH-Ricci} = A_\Delta \dot{R}\left[1 - \frac{\Delta}{2}(\ln\bar{R} + 1)\right], \tag{114}$$

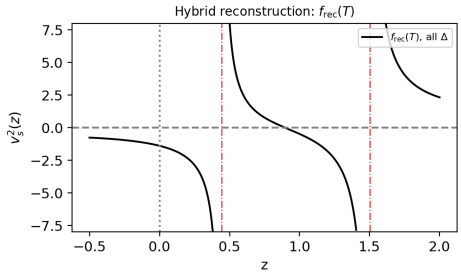
$$\ddot{\rho}_{\rm BH-Ricci} = A_\Delta\left\{\ddot{R}\left[1 - \frac{\Delta}{2}(\ln\bar{R} + 1)\right] - \frac{\Delta}{2}\frac{\dot{R}^2}{R}\right\}, \tag{115}$$

$$\dot{\rho}_{\rm GDE} = \alpha\dot{H}, \qquad \ddot{\rho}_{\rm GDE} = \alpha\ddot{H}. \tag{116}$$

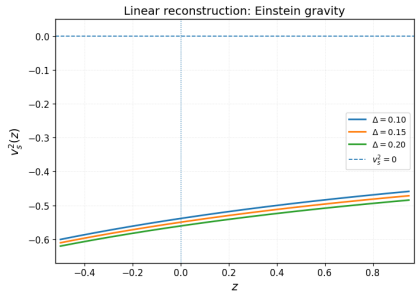
The derivatives are evaluated only where $R > 0$, as required by the logarithmic prescription. The density and its derivatives in this Einstein-gravity diagnostic therefore retain their explicit dependence on Δ.



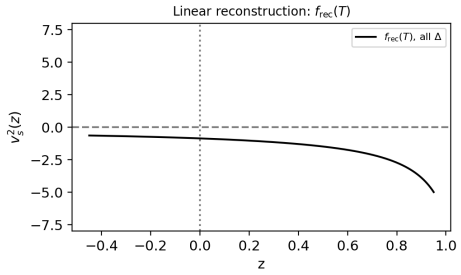
(**a**) Einstein gravity



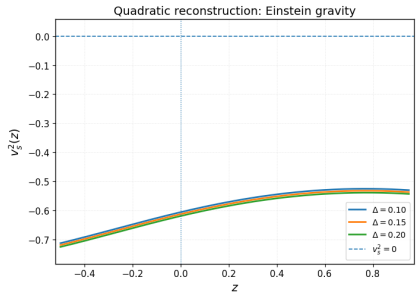
(**b**) $f(T)$ gravity



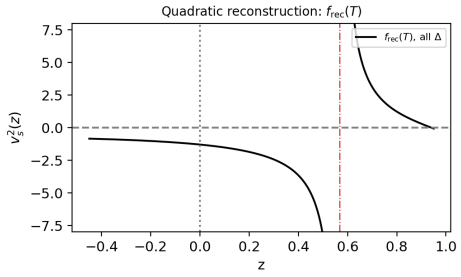
(**c**) Einstein gravity



(**d**) $f(T)$ gravity



(**e**) Einstein gravity



(**f**) $f(T)$ gravity

Figure 10. Squared-sound-speed diagnostic $v_s^2(z)$ for the three scale-factor backgrounds. The upper, middle, and lower rows correspond to the hybrid, linear, and quadratic cases; the left and right columns show the Einstein-gravity and reconstructed $f(T)$ calculations, respectively. The right-column curves are computed for the reconstructed function $f_{\rm rec}(T)$ using $\rho_{\rm DE}^{\rm tot} = 3H^2 - \rho_m$ in units $H_0 = M_{\rm Pl} = 1$; they are therefore independent of Δ. In the right column, vertical dash-dotted lines mark the zeros of $d\rho_{\rm DE}^{\rm tot}/dz$, where the adiabatic diagnostic v_s^2 has poles; all such roots in the displayed redshift range are included. The left-column curves correspond to $\Delta = 0.10$, 0.15, and 0.20. Negative values indicate a warning sign for the effective-fluid description, not by themselves a proof of instability of the underlying $f(T)$ theory.

For the reconstructed $f_{\rm rec}(T)$ curves (right column of Figure 10), we use the effective density fixed by the first Friedmann equation,

$$\rho_{\rm DE}^{\rm tot} = 3M_{\rm Pl}^2 H^2 - \rho_m, \qquad \rho_m = 3M_{\rm Pl}^2 H_0^2 \Omega_{m0}(1+z)^3. \tag{117}$$

This is equivalent to including the torsional contribution defined by $\rho_T = 3M_{\rm Pl}^2 H^2 - \rho_m - \rho_{\rm BH-Ricci} - \rho_{\rm GDE}$. Consequently, the reconstructed effective density is fixed by $H(z)$

and the adopted matter density; it is not obtained by substituting the power-law ansatz $T + \beta(-T)^m$ for $f_{\rm rec}(T)$. Its derivatives are

$$\dot{\rho}_{\rm DE}^{\rm tot} = 6M_{\rm Pl}^2 H\dot{H} + 3H\rho_m, \tag{118}$$

$$\ddot{\rho}_{\rm DE}^{\rm tot} = 6M_{\rm Pl}^2(\dot{H}^2 + H\ddot{H}) + 3\dot{H}\rho_m - 9H^2\rho_m. \tag{119}$$

These expressions depend on the CC-constrained expansion history and the fixed matter fraction and hence are independent of Δ. Varying Δ changes the split between the explicit source and the reconstructed torsional term, not this total effective density.

For either choice of density, the effective pressure is defined through the continuity relation,

$$p_{\rm DE} = -\rho_{\rm DE} - \frac{\dot{\rho}_{\rm DE}}{3H}. \tag{120}$$

Thus

$$v_s^2 = \frac{\dot{p}_{\rm DE}}{\dot{\rho}_{\rm DE}}, \qquad \dot{\rho}_{\rm DE} \neq 0. \tag{121}$$

Using $dz/dt = -(1+z)H$, this can be evaluated directly as

$$p_{\rm DE}(z) = -\rho_{\rm DE}(z) + \frac{1+z}{3}\frac{d\rho_{\rm DE}}{dz}, \tag{122}$$

$$v_s^2(z) = \frac{dp_{\rm DE}/dz}{d\rho_{\rm DE}/dz} = \frac{(1+z)\,d^2\rho_{\rm DE}/dz^2 - 2\,d\rho_{\rm DE}/dz}{3\,d\rho_{\rm DE}/dz}, \qquad \frac{d\rho_{\rm DE}}{dz} \neq 0. \tag{123}$$

This numerical form follows directly from the definition. Points at which the density derivative vanishes are excluded because the ratio has a pole there. For the reconstructed total sector, these points correspond to $w_{\rm DE}^{\rm tot} = -1$ when the density is nonzero.

The CC-constrained parameters (H_0, p, n) are used separately for the hybrid, linear, and quadratic histories. We fix $c = 1.2$ and $\Omega_{m0} = 0.30$ and consider $\Delta = 0.10$, 0.15, and 0.20 for the Einstein-gravity calculation. The power-law form $f_{\rm PL}(T) = T + \beta(-T)^m$ with $m = 0.32$ is assessed only through the background residuals in Section 6; it is not used to calculate the right-column stability curves. The sign of v_s^2 is interpreted only as an effective-fluid diagnostic: a negative value is a warning about this background description, not proof of instability in the underlying modified-gravity theory.

For the hybrid background, the general time-domain expression can also be written as

$$v_s^2(t) = -1 - \frac{\ddot{\rho}_{\rm DE}}{3H\dot{\rho}_{\rm DE}} + \frac{\dot{H}}{3H^2}. \tag{124}$$

Since $H = \psi + n/t$ and $\dot{H} = -n/t^2$ for this scale factor,

$$v_s^2(t) = -1 - \frac{\ddot{\rho}_{\rm DE}}{3(\psi + n/t)\dot{\rho}_{\rm DE}} - \frac{n}{3t^2(\psi + n/t)^2}. \tag{125}$$

The sign depends on the density derivatives and the background. It cannot be inferred from the scale factor alone.

The left-column $v_s^2(z)$ curves use the first-order BH–Ricci density and the ghost density, so they depend on Δ. The right-column curves use $\rho_{\rm DE}^{\rm tot} = 3M_{\rm Pl}^2H^2 - \rho_m$ for the reconstructed function and are independent of Δ. The power-law coefficient β does not enter these reconstructed-function curves.

Using $\rho_{\rm DE}^{\rm tot} = 3M_{\rm Pl}^2H^2 - \rho_m$, the present-day values obtained from the CC best-fit backgrounds are $v_s^2(0) \simeq -1.39$, -0.86, and -1.30 for the hybrid, linear, and quadratic histories, respectively. Over $-0.8 \leq z \leq 2.5$, zeros of $d\rho_{\rm DE}^{\rm tot}/dz$ occur near $z = 0.444$ and 1.500 for the hybrid history, $z = 1.107$ and 2.275 for the linear history, and $z = 0.568$ and

1.412 for the quadratic history. The sound-speed ratio has poles at these points, which are marked in the right-column plots. The diagnostic is an adiabatic effective-fluid ratio and does not by itself establish stability or instability of the underlying $f(T)$ theory.

In Figure 10, the reconstructed effective-fluid diagnostic indicates that $v_s^2 < 0$ at the present epoch for all three best-fit expansion histories. Its evolution may also exhibit singular behavior when the time derivative of the effective energy density vanishes. The sign of v_s^2 provides a diagnostic of the effective-fluid description and, by itself, does not establish the full perturbative stability or instability of the underlying $f(T)$ gravity model.

The ratio $\dot{p}/\dot{\rho}$ is an adiabatic background diagnostic. For a multi-component effective sector it need not equal the rest-frame perturbation sound speed; a canonical scalar field, for example, can have $\dot{p}/\dot{\rho} < 0$ while its rest-frame sound speed is positive. Its sign is therefore used only to assess the adiabatic effective-fluid description. Points near the poles of $\dot{p}/\dot{\rho}$, where $d\rho_{\rm DE}^{\rm tot}/dz = 0$, are excluded.

8. *Om* and Statefinder Diagnostics

We use the *Om* and Statefinder diagnostics to compare the reconstructed expansion histories with the ΛCDM reference model [76–78]. These are geometrical diagnostics rather than independent stability criteria. Their asymptotic behavior is first determined from the three scale factors. For the hybrid scale factor, $a_{\rm H}(t) = e^{\psi t}t^n$, the exponential term dominates at late times. Thus $H \to \psi$, $q \to -1$, and $(r, s) \to (1, 0)$. The linear and quadratic truncations instead approach power laws, $a_{\rm L}(t) \propto t^{n+1}$ and $a_{\rm Q}(t) \propto t^{n+2}$. Their deceleration and Statefinder parameters therefore approach constants that generally differ from the de Sitter values. This difference should be kept in mind when reading the diagnostics below.

The Om diagnostic is defined as [78]

$$Om(z) = \frac{H^2(z)/H_0^2 - 1}{(1+z)^3 - 1}, \tag{126}$$

where $H(z)$ is the Hubble parameter and H_0 is its present value. For spatially flat ΛCDM, $Om(z) = \Omega_{m0}$ is constant. For flat GR with conserved dust and constant dark-energy w, a negative slope of $Om(z)$ with respect to z is associated with quintessence-like behavior ($w > -1$) and a positive slope with phantom-like behavior ($w < -1$) [78]. This rule cannot be applied indiscriminately to time-varying effective fluids or modified gravity, so $Om(z)$ is used here mainly as a null test of the expansion history. The limit $z \to 0$ is removable: $Om(0) = \frac{2}{3}(1 + q_0)$, which gives 0.373, 0.539 and 0.414 for the hybrid, linear and quadratic histories.

Figure 11 shows $Om(z)$ for the hybrid, linear, and quadratic histories. This quantity tests the expansion history against the flat ΛCDM reference; it does not directly determine the dark-energy equation of state, which is calculated separately.

We also study the Statefinder diagnostic, which is defined by the parameters [76,77]

$$r = \frac{\dddot{a}}{aH^3}, \qquad s = \frac{r-1}{3\left(q - \frac{1}{2}\right)}, \tag{127}$$

where a is the scale factor, H is the Hubble parameter, and q is the deceleration parameter. The Statefinder pair (r, s) distinguishes different expansion histories; flat ΛCDM corresponds to the fixed point $(r, s) = (1, 0)$.

The Statefinder trajectories distinguish the three reconstructed histories from the ΛCDM reference at finite redshift. Only the hybrid reconstruction approaches the de Sitter fixed point $(r, s) = (1, 0)$ at late times; the linear and quadratic truncations have power-law asymptotics and therefore approach model-dependent limits in general. The geometrical

diagnostics should thus be interpreted as comparisons with ΛCDM rather than independent proofs of stability.

Figure 11 presents the Om diagnostic for the hybrid, linearly truncated, and quadratically truncated reconstructions over $0 \leq z \leq 2$. The three reconstruction schemes show smooth model-dependent $Om(z)$ evolutions. At the present epoch, $Om(0) \simeq 0.373$, 0.539, and 0.414 for the hybrid, linear, and quadratic histories, respectively; hence the linear history has the largest present-day offset from the flat ΛCDM reference $Om = \Omega_{m0} = 0.30$. All three curves initially have a negative slope with redshift. Over the displayed interval $0 \leq z \leq 2$, the hybrid and quadratic curves flatten and turn slightly upward at $z \gtrsim 1.4$. These trends identify finite-redshift departures from the reference expansion history; the present analysis does not assign a more precise redshift of maximum deviation without a dedicated numerical maximization of $|Om(z) - 0.30|$. The Om diagnostic therefore quantifies deviations from the ΛCDM expansion history.

We also use the Statefinder parameters

$$r = 1 + 3\frac{\dot{H}}{H^2} + \frac{\ddot{H}}{H^3}, \tag{128}$$

and

$$s = \frac{r - 1}{3\left(q - \frac{1}{2}\right)}, \qquad q = -1 - \frac{\dot{H}}{H^2}. \tag{129}$$

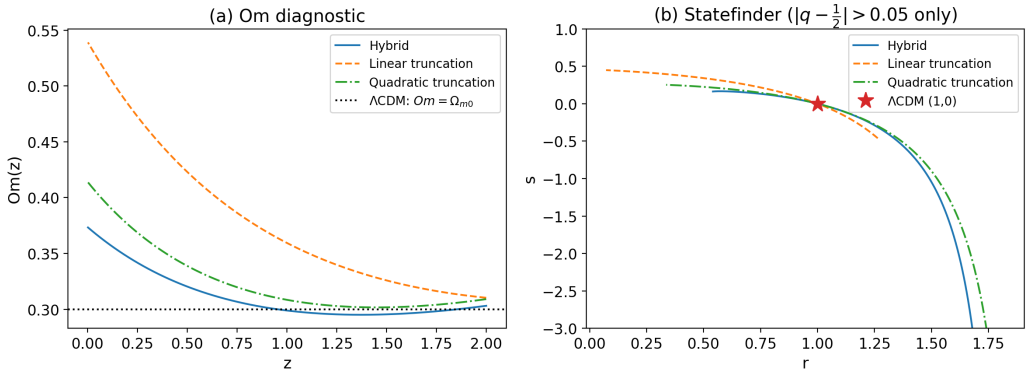


Figure 11. Geometrical diagnostics of the reconstructed history of expansion. In the left panel we show the Om diagnostic $Om(z)$ for the hybrid, linearly truncated and quadratically truncated scale-factor prescriptions. The horizontal reference line corresponds to the flat ΛCDM value $Om = \Omega_{m0} = 0.30$. The corresponding Statefinder trajectories in the (r, s) plane are shown in the right panel. The ΛCDM fixed point $(r, s) = (1, 0)$ is marked with a star; points with $|q - 1/2| < 0.05$ are excluded from the (r, s) curves.

Figure 11 shows the geometrical diagnostics of the reconstructed expansion histories. In the left panel, the three scale-factor reconstructions deviate from the reference ΛCDM behavior, $Om = \Omega_{m0} = 0.30$, in the relevant redshift range. The right panel shows the corresponding trajectories in the (r, s) plane, with the ΛCDM fixed point $(r, s) = (1, 0)$ indicated for reference. The three reconstructions follow different paths and hence have quantitatively different expansion histories. The hybrid reconstruction approaches the de Sitter limit and hence the ΛCDM Statefinder fixed point $(r, s) = (1, 0)$ at late times, whereas the linearly and quadratically truncated scale factors have power-law asymptotics and therefore approach model-dependent constant Statefinder values in general. The large excursions of s at high redshift are produced by the denominator $q - \frac{1}{2}$ in Equation (129), which vanishes at $z_q \simeq 2.05$, 2.81 and 2.02 for the hybrid, linear and quadratic histories; they are not physical features, and the plotted (r, s) curves exclude $|q - \frac{1}{2}| < 0.05$.

The deviation of $Om(z)$ from the present-day matter density parameter, $\Omega_{m0} = 0.30$, is evident in Figure 11 for all three scale factors. After a monotone decreasing pattern, the hybrid and quadratic models show a flattening followed by a mildly upward trend at higher redshifts ($z \gtrsim 1.4$). The Statefinder trajectories also differ among the models. However, the exact redshifts at which the maximum deviations from the ΛCDM model occur have not been determined numerically. These diagnostics indicate differences in the background evolution. However, they do not establish an observational preference based on this behavior alone.

In summary, while the Om and Statefinder diagnostics effectively quantify finite-redshift deviations from the standard ΛCDM expansion history, they rely strictly on the prescribed kinematics of the scale factors. Because they do not independently test the underlying modified field-equation dynamics or local stability constraints of $f(T, B)$ gravity, they serve primarily as geometrical comparisons rather than an independent criterion for observational preference.

9. Generalized Second Law of Thermodynamics

The generalized second law of thermodynamics (GSL) provides a thermodynamic consistency test for cosmological models with horizons [79–85]. It requires the total entropy of the horizon and the matter–energy inside it to be non-decreasing with cosmic time [86–89]. Related analyses have been performed in modified gravity and dark-energy models [48,89–97]. Shekh et al. [98] examined Tsallis holographic dark energy in $f(T, B)$ gravity, including energy conditions and the generalized second law. Ref. [98] provides a useful precedent for the thermodynamic part of the current analysis while allowing us to distinguish our $f(T)$ reconstruction and Barrow–Ricci prescription from their framework. As the thermodynamic framework, we use the equilibrium formulation in which the $f(T)$ field equations are written in Einstein form with the effective torsional density and pressure of Equations (86) and (87), as in Ref. [99]. The total effective fluid then satisfies $\rho + p = -2M_{\rm Pl}^2\dot{H}$. Therefore, the torsional contribution enters $\dot{S}_m$ through $\rho + p$. All the components are assumed to be in equilibrium at the Hubble horizon temperature $T_h = 1/(2\pi R_h)$. In a flat FLRW universe the Hubble and apparent horizons coincide, $R_A = 1/H$. Thus the only difference is the temperature definition. For the dynamical apparent-horizon temperature $T_A = (1-q)H/(4\pi)$ the fluid term is rescaled, $\dot{S}_m \to 2\dot{S}_m/(1-q)$. This is used as a check. A non-equilibrium treatment would add an f_T-dependent horizon entropy and an internal entropy-production term [99]; these are not included here.

Here,

$$\dot{S}_{\rm total} = \dot{S}_{\rm horizon} + \dot{S}_{\rm matter/fluid} \geq 0.$$

For the Barrow entropy prescription,

$$\dot{S}_{\rm total} = \dot{S}_B + \dot{S}_m \geq 0,$$

where $\dot{S}_B$ and $\dot{S}_m$ are the horizon and matter/fluid entropy-production rates, respectively.

The Barrow entropy is defined as

$$S_B = \gamma A^{1+\frac{\Delta}{2}},$$

where $A = 4\pi R_h^2$ is the horizon area, R_h is the radius of the horizon, Δ is the Barrow deformation parameter, and γ is a constant.

Explicitly, this gives

$$S_B = 4\pi\gamma(4\pi)^{\frac{\Delta}{2}} R_h^{2+\Delta}.$$

Taking the time derivative gives

$$\dot{S}_B = 4\pi\gamma(\Delta+2)(4\pi)^{\frac{\Delta}{2}}(R_h)^{1+\Delta}\dot{R}_h \tag{130}$$

The temperature at the horizon is given by

$$T_h = \frac{1}{2\pi R_h} \tag{131}$$

Now, for the fluid inside the horizon, using the Gibbs relation,

$$T_h dS_m = dE_m + pdV, \tag{132}$$

where E_m is the energy of the fluid inside the horizon, given by $E_m = \rho V$, and V is the horizon volume: $V = \frac{4}{3}\pi R_h^3$.

Taking the time derivative of Equation (132) we obtain:

$$T_h \dot{S}_m = V\dot{\rho} + (p+\rho)\dot{V}. \tag{133}$$

Now, using the energy conservation equation

$$\dot{\rho} + 3H(\rho + p) = 0,$$

in Equation (133) gives

$$T_h \dot{S}_m = 4\pi R_h^2(\rho + p)(\dot{R}_h - HR_h),$$

which simplifies to

$$\dot{S}_m = 8\pi^2 R_h^3(\rho + p)(\dot{R}_h - HR_h) \tag{134}$$

where ρ and p denote the effective density and effective pressure, respectively.

Validation of the Generalized Second Law of Thermodynamics at the Hubble Horizon

We test the generalized second law (GSL) at the Hubble horizon by evaluating the total entropy-production rate for the three reconstructed scale factors. This is a test of the GSL within the adopted effective thermodynamic description, and it is distinct from perturbative stability of the underlying $f(T)$ theory.

For the Hubble horizon, we take the infrared cutoff to be

$$L = R_h = \frac{1}{H},$$

where R_h is the horizon radius.

Using Equation (130), the Barrow entropy-production rate at the Hubble horizon is

$$\dot{S}_B = -4\pi\gamma(\Delta+2)(4\pi)^{\frac{\Delta}{2}}\frac{\dot{H}}{H^{3+\Delta}} \tag{135}$$

Using Equation (134), the entropy-production rate of the matter/fluid inside the Hubble horizon is

$$\dot{S}_m = -8\pi^2(\rho + p)\left(\frac{\dot{H}}{H^5} + \frac{1}{H^3}\right) \tag{136}$$

Adding Equations (135) and (136) gives the total entropy-production rate at the Hubble horizon, in which the pressureless matter is included explicitly through $\rho + p = \rho_m + \rho_{\rm DE}^{\rm tot}(1 + w_{\rm DE}^{\rm tot})$

$$\dot{S}_{\rm total} = \dot{S}_B + \dot{S}_m = -4\pi\gamma(\Delta+2)(4\pi)^{\frac{\Delta}{2}}\frac{\dot{H}}{H^{3+\Delta}} - 8\pi^2\left[\rho_m + \rho_{\rm DE}^{\rm tot}(1+w_{\rm DE}^{\rm tot})\right]\left(\frac{\dot{H}}{H^5} + \frac{1}{H^3}\right), \tag{137}$$

where $\rho_{\rm DE}^{\rm tot}$ is defined in Equation (93) and $w_{\rm DE}^{\rm tot}$ in Equation (95). For the reconstructed background, we define $\rho_{\rm DE}^{\rm tot} = 3M_{\rm Pl}^2H^2 - \rho_m$. Under this effective-fluid definition, the continuity relation gives $\rho_m + \rho_{\rm DE}^{\rm tot}(1 + w_{\rm DE}^{\rm tot}) = -2M_{\rm Pl}^2\dot{H}$. With $M_{\rm Pl} = 1$, the matter–fluid contribution becomes $\dot{S}_m = 16\pi^2\dot{H}(\dot{H} + H^2)/H^5$. For $\Delta \to 0$, the Barrow entropy reduces to the area law, $S_B = \gamma A$. With $\gamma = 2\pi$ in units $M_{\rm Pl}^2 = 1$, this recovers the Bekenstein–Hawking entropy. In this limit, Equation (137) gives $\dot{S}_{\rm total} = 16\pi^2\dot{H}^2/H^5 \geq 0$ under the adopted Einstein-form effective-fluid prescription. The generalized second law is examined within this equilibrium prescription and does not constitute a general thermodynamic validation of the full $f(T)$ gravity theory. The rates are expressed in units with $H_0 = 1$.

This is the equilibrium Einstein-form effective-fluid formulation in which all the components share the horizon temperature $T_h = 1/(2\pi R_h)$. No f_T-dependent correction to the horizon entropy or internal entropy-production term is included, so the result is a GSL test of this effective description, not a test of a full non-equilibrium $f(T)$ thermodynamics. For $\Delta = 0$, $S_B = \gamma A$ reduces to the Bekenstein–Hawking law when $\gamma = 1/(4G)$, which equals 2π in units $M_{\rm Pl}^2 = 1/(8\pi G) = 1$; the adopted $\gamma = 6.0$ is close to this value. For $\Delta = 0$ and $\gamma = 2\pi$, Equation (137) reduces to $\dot{S}_{\rm total} = 16\pi^2\dot{H}^2/H^5 \geq 0$, as expected in Einstein gravity. Rates are given in units $H_0 = 1$.

Figure 12 shows $\dot{S}_B$, $\dot{S}_m$ and $\dot{S}_{\rm total}$ as functions of redshift for the three reconstructed scale factors and $\Delta = 0.10$, 0.15, and 0.20. The calculations use the CC-constrained background parameters; $\gamma = 6.0$ is kept fixed for all Δ and all histories. Over $0 \leq z \leq 0.95$ the matter–fluid term $\dot{S}_m$ is negative at low redshift (down to about -39, -24 and -37 at $z = 0$ for the hybrid, linear and quadratic histories), whereas $\dot{S}_B > 0$, so the sign of the sum depends on γ; it is not merely an overall normalization. For $\gamma = 6.0$, $\dot{S}_{\rm total} > 0$ throughout, with minimum values of about 62 (hybrid), 98 (linear) and 74 (quadratic) at $\Delta = 0.10$. Positivity over the whole interval requires $\gamma \gtrsim 2.3$, 1.0 and 2.0 for the hybrid, linear and quadratic histories at $\Delta = 0.10$ ($\gamma \gtrsim 1.95$, 0.85 and 1.7 at $\Delta = 0.20$); both $\gamma = 6.0$ and the Bekenstein–Hawking value $\gamma = 2\pi$ lie above these thresholds. Within this effective-fluid description the generalized second law is therefore satisfied at the Hubble horizon on $0 \leq z \leq 0.95$ for the reconstructed model. As a check on the horizon temperature, we replaced T_h by the apparent-horizon temperature $T_A = (1-q)H/(4\pi)$. Since $q < 1$ on $0 \leq z \leq 0.95$ ($q \lesssim 0.09$), $T_A > 0$ throughout. The fluid term becomes more negative: $\dot{S}_m(0) \simeq -54$, -41 and -54 for the hybrid, linear and quadratic histories at $\Delta = 0.10$. The total rate remains positive for $\gamma = 6.0$ and $\gamma = 2\pi$ (minimum values about 47, 97 and 58 at $\gamma = 6.0$). The thresholds rise to $\gamma \gtrsim 3.2$, 1.7 and 2.9 at $\Delta = 0.10$ and 2.7, 1.4 and 2.4 at $\Delta = 0.20$. The conclusion is therefore unchanged by the choice of horizon temperature. We do not repeat the entropy calculation with the power-law torsional density since it does not satisfy the background field equations.

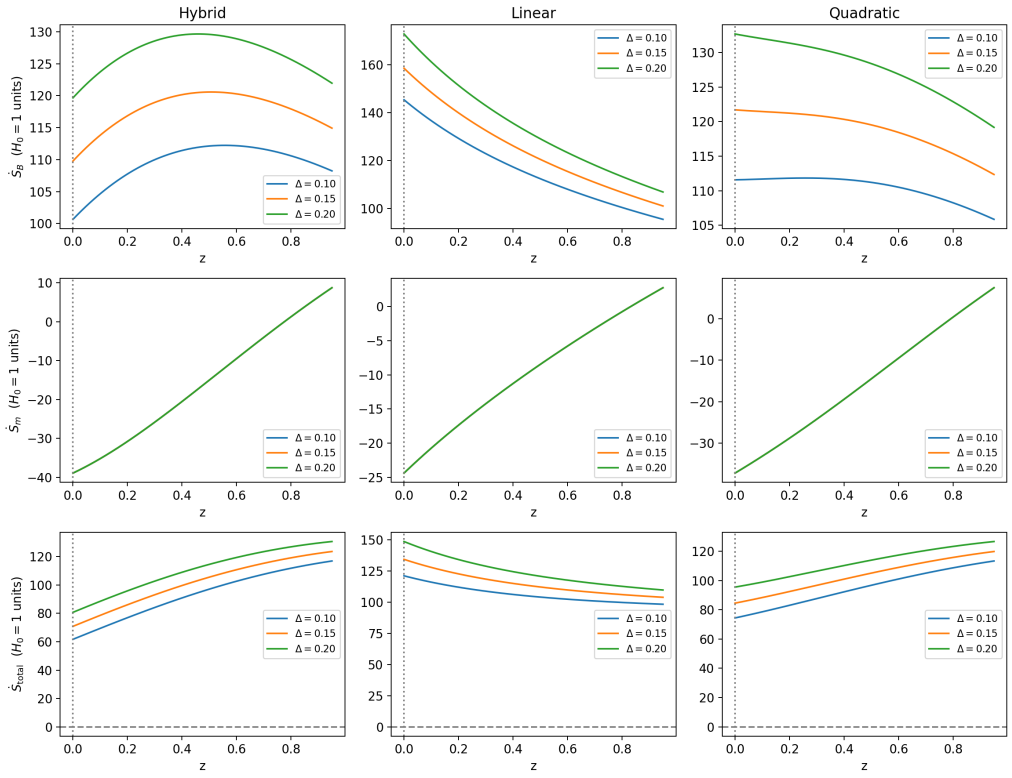


Figure 12. Entropy-production rates for the Barrow horizon, $\dot{S}_B$, the effective matter–fluid component, $\dot{S}_m$, and the total $\dot{S}_{\rm total} = \dot{S}_B + \dot{S}_m$ for the three CC-constrained scale-factor backgrounds. The rates are evaluated from Equation (137) with the matter contribution included, $\gamma = 6.0$, and $H_0 = 1$ units. They refer to the stated equilibrium effective-fluid prescription, not a separate non-equilibrium $f(T)$ entropy calculation. Curves correspond to $\Delta = 0.10$, 0.15, and 0.20. The horizontal dashed line in the bottom row marks zero entropy production.

10. Comparative Remarks

The results from the three prescribed scale-factor histories are summarized in Table 5. All three prescribed backgrounds exhibit a deceleration-to-acceleration transition over the relevant range. The geometrical effective equation of state varies with redshift and can cross both the phantom divide and the acceleration boundary; it should therefore be interpreted only as the effective-fluid diagnostic defined in Figure 9. The main differences appear in the detailed evolution of the expansion rate and the late-time asymptotics. The hybrid form keeps its exponential factor and therefore approaches a de Sitter-like behavior at sufficiently late times, whereas the linear and quadratic truncations asymptotically approach power-law forms.

The three prescriptions should not be ranked using the effective-fluid stability diagnostic alone. The squared sound speed in Equation (121) is an adiabatic diagnostic of the effective-fluid description; regions with $v_s^2 < 0$ signal that the adiabatic effective-fluid description is not reliable there. This is not a complete perturbative stability analysis of the underlying $f(T)$ theory. The reconstructed-function sound-speed values are negative at $z = 0$ for the three CC best-fit histories. The entropy-production rate at the Hubble horizon is positive for $\gamma = 6.0$ within the equilibrium effective-fluid prescription; this conclusion depends on the adopted entropy normalization and does not establish the thermodynamics of the full non-equilibrium $f(T)$ theory.

The geometrical diagnostics provide an additional comparison of the reconstructed expansion histories. Figure 11 shows the $Om(z)$ deviations from the flat ΛCDM reference value and the corresponding Statefinder trajectories. The hybrid model approaches the fixed

point $(r, s) = (1, 0)$ in its late-time de Sitter limit, whereas the linear and quadratic truncations have power-law asymptotics and therefore need not approach the same fixed point.

Approach I and Approach II have different physical interpretations. Approach I treats the BH–Ricci and QCD ghost terms as additive contributions to the effective dark-energy sector. Approach II imposes the correspondence $\rho_{\rm BHDE} = \rho_{\rm GDE}$ and therefore uses a single effective component. The exact correspondence yields the constant-Hubble exponential solution. The linear and quadratic forms are retained as phenomenological Taylor-truncated histories used to test sensitivity to the expansion order; because their Hubble rates vary with time, they do not preserve the exact BHDE–GDE density equality away from the normalization point. Their EoS curves therefore reflect the adopted fixed reference density rather than exact solutions of the correspondence. Neither construction is assumed to be universally superior; the comparison shows how quantitative evolution depends on the reconstruction prescription.

Table 5. Summary of the principal cosmological and thermodynamic features of the three scale-factor prescriptions.

Case	Scale Factor	Characteristic Behavior	Consistency Diagnostics
Case I	$a(t) = e^{\psi t} t^n$	Smooth transition from early deceleration to late-time de Sitter-like expansion.	Reconstructed $f(T)$: residuals $\lesssim 10^{-8}$; $v_s^2(0) \simeq -1.39$; poles at $z \simeq 0.444, 1.500$; $\dot{S}_{\rm total} > 0$ for $\gamma \gtrsim 2.3$ ($\Delta = 0.10$).
Case II	$a(t) = (1 + \psi t) t^n$	Linear truncation of the hybrid form with power-law late-time asymptotics.	Reconstructed $f(T)$: residuals $\lesssim 10^{-9}$; $v_s^2(0) \simeq -0.86$; poles at $z \simeq 1.107, 2.275$; $\dot{S}_{\rm total} > 0$ for $\gamma \gtrsim 1.0$ ($\Delta = 0.10$).
Case III	$a(t) = \left(1 + \psi t + \frac{\psi^2 t^2}{2}\right) t^n$	Quadratic truncation retaining the next-order correction to the exponential factor.	Reconstructed $f(T)$: residuals $\lesssim 10^{-8}$; $v_s^2(0) \simeq -1.30$; poles at $z \simeq 0.568, 1.412$; $\dot{S}_{\rm total} > 0$ for $\gamma \gtrsim 2.0$ ($\Delta = 0.10$).

Comparison with the ΛCDM Model

The ΛCDM model is used here as a geometrical reference rather than an exact limit of every reconstructed scale factor. The Om diagnostic in Figure 11 shows deviations from the reference value $Om = \Omega_{m0} = 0.30$ over finite redshift. The Statefinder pair provides a further distinction: the ΛCDM model corresponds to the fixed point $(r, s) = (1, 0)$, which is approached by the hybrid reconstruction in its late-time de Sitter regime. The linear and quadratic truncations instead have power-law asymptotics, so their Statefinder limits are generally model-dependent. Thus, the hybrid model approaches the ΛCDM Statefinder limit at late times, whereas the linear and quadratic models generally do not.

11. Concluding Remarks

In this work, we studied a dark-energy model that combines Barrow–Ricci holographic dark energy with QCD ghost dark energy and reconstructed an effective $f(T)$ description. The hybrid, linear, and quadratic scale-factor histories were fitted to the Cosmic Chronometer data using the likelihood in Equation (50). The best-fit values are listed in Table 1, and the corresponding Hubble curves are compared with the measurements in Figure 1. The information criteria in Table 2 favor flat ΛCDM among the compared models, although the differences for the three kinematic histories are modest. The reconstructed EoS and deceleration histories are shown in Figures 3 and 6; they indicate late-time acceleration over the redshift ranges that were studied. We considered two prescriptions for the dark-energy sector. In Approach I, the Barrow–Ricci and ghost contributions are added. In Approach II, we impose the correspondence $\rho_{\rm BHDE} = \rho_{\rm GDE}$, which gives a constant-H

solution for the exact Hubble-cutoff case, while the linear and quadratic histories are truncated forms. Their EoS behavior is compared in Figure 5. The comparison shows that the inferred evolution depends on the chosen prescription and background history; the two constructions should not be treated as equivalent.

For the effective $f(T)$ reconstruction, we used the solution specified by Equation (100) and evaluated the normalized residuals associated with Equations (102) and (103). The first-equation residuals are shown in Figure 7. Their maxima are summarized in Table 4. The pressure used in the second residual is obtained from the continuity relation, so that residual is a numerical consistency check within the adopted prescription, not an independent physical test. The power-law form $f_{\rm PL}(T) = T + \beta(-T)^m$, tested with $m = 0.32$ and present-day normalization, gives appreciable residuals away from the normalization point (Figure 8 and Table 4). Thus, this normalization alone does not make the power-law form consistent with all three prescribed histories.

We also examined the effective-fluid sound speed defined in Equation (121). Its present-day value is negative for all three CC best-fit histories, and poles occur where the redshift derivative of the effective density vanishes; these features are displayed in Figure 10. This quantity is a background effective-fluid diagnostic. It does not, by itself, establish the perturbative stability or instability of the underlying $f(T)$ theory. The geometrical diagnostics in Figure 11 show departures from the flat ΛCDM reference. The hybrid history approaches the Statefinder point $(r, s) = (1, 0)$ at late times, whereas the linearly and quadratically truncated histories have power-law asymptotics and need not approach that point. These diagnostics are useful for comparing the expansion histories, but they do not independently establish dynamical stability.

Finally, we evaluated the entropy-production rate using the total-rate expression in Equation (137). For the adopted equilibrium effective-fluid prescription, the total rate is positive over $0 \leq z \leq 0.95$ for $\gamma = 6.0$; at $\Delta = 0.10$, the corresponding threshold values of γ are approximately 2.3, 1.0, and 2.0 for the hybrid, linear, and quadratic histories, respectively. The evolution is shown in Figure 12. This conclusion applies to the Barrow horizon entropy and matter contribution used here; it does not include additional f_T-dependent horizon-entropy corrections or a non-equilibrium production term.

We propose that future research should examine perturbations of the gravitational degrees of freedom and include possible f_T-dependent entropy terms. The observational constraints could also be revisited by combining CC measurements with Type Ia supernova, BAO, and CMB data and taking into account the full covariance of the CC measurements.

Author Contributions: Conceptualization, S.C.; methodology, B.C. and S.C.; software, B.C.; validation, I.G.S. and S.C.; formal analysis, B.C. and I.G.S.; investigation, B.C.; writing—original draft preparation, B.C.; writing—review and editing, I.G.S. and S.C.; visualization, B.C.; supervision, S.C. All authors have read and agreed to the published version of the manuscript.

Funding: This research received no external funding.

Data Availability Statement: The Cosmic Chronometer data used in this study are publicly available through the compilation cited as Ref. [68]. No new observational dataset was generated in this study.

Acknowledgments: The authors sincerely acknowledge the constructive suggestions from the anonymous reviewers. The third author, Surajit Chattopadhyay, acknowledges the Visiting Associateship of the Inter-University Centre for Astronomy and Astrophysics (IUCAA), Pune, India.

Conflicts of Interest: The authors declare no conflict of interest.

References

1. Riess, A.G.; Filippenko, A.V.; Challis, P.; Clocchiatti, A.; Diercks, A.; Garnavich, P.M.; Gilliland, R.L.; Hogan, C.J.; Jha, S.; Kirshner, R.P.; et al. Observational Evidence from Supernovae for an Accelerating Universe and a Cosmological Constant. *Astron. J.* **1998**, *116*, 1009–1038. https://doi.org/10.1086/300499.
2. Perlmutter, S.; Aldering, G.; Goldhaber, G.; Knop, R.A.; Nugent, P.; Castro, P.G.; Deustua, S.; Fabbro, S.; Goobar, A.; Groom, D.E.; et al. Measurements of Ω and Λ from 42 High-Redshift Supernovae. *Astrophys. J.* **1999**, *517*, 565–586. https://doi.org/10.1086/307221.
3. Aghanim, N. et al. [Planck Collaboration]. Planck 2018 results. VI. Cosmological parameters. *Astron. Astrophys.* **2020**, *641*, A6 . https://doi.org/10.1051/0004-6361/201833910.
4. Eisenstein, D.J.; Zehavi, I.; Hogg, D.W.; Scoccimarro, R.; Blanton, M.R.; Nichol, R.C.; Scoccimarro, R.; Seo, H.-J.; Tegmark, M.; Zheng, Z.; et al. Detection of the baryon acoustic peak in the large-scale correlation function of SDSS luminous red galaxies. *Astrophys. J.* **2005**, *633*, 560–574. https://doi.org/10.1086/466512.
5. Mortonson, M.J.; Weinberg, D.H.; White, M. Dark Energy: A Short Review. *arXiv* **2014**, arXiv:1401.0046.
6. Weinberg, S. The Cosmological Constant Problem. *Rev. Mod. Phys.* **1989**, *61*, 1–23. https://doi.org/10.1103/RevModPhys.61.1.
7. Nojiri, S.; Odintsov, S.D. Modified gravity as an alternative for ΛCDM cosmology. *J. Phys. A Math. Theor.* **2007**, *40*, 6725–6732. https://doi.org/10.1088/1751-8113/40/25/S17.
8. Tsujikawa, S. Quintessence: A Review. *Class. Quantum Gravity* **2013**, *30*, 214003. https://doi.org/10.1088/0264-9381/30/21/214003.
9. Copeland, E.J.; Sami, M.; Tsujikawa, S. Dynamics of Dark Energy. *Int. J. Mod. Phys. D* **2006**, *15*, 1753–1936. https://doi.org/10.1142/S021827180600942X.
10. Nojiri, S.; Odintsov, S.D. Unified cosmic history in modified gravity: From $F(R)$ theory to Lorentz non-invariant models. *Phys. Rep.* **2011**, *505*, 59–144. https://doi.org/10.1016/j.physrep.2011.04.001.
11. Bamba, K.; Capozziello, S.; Nojiri, S.; Odintsov, S.D. Dark energy cosmology: The equivalent description via different theoretical models and cosmography tests. *Astrophys. Space Sci.* **2012**, *342*, 155–228. https://doi.org/10.1007/s10509-012-1181-8.
12. Nojiri, S.; Odintsov, S.D. Unifying phantom inflation with late-time acceleration. In *General Relativity and Gravitation*; Springer: New York, NY, USA, 2006; Volume 38, pp. 1285–1304. https://doi.org/10.1007/s10714-006-0301-6.
13. Nojiri, S.; Odintsov, S.D. Covariant generalized holographic dark energy and accelerating universe. *Eur. Phys. J. C* **2017**, *77*, 528. https://doi.org/10.1140/epjc/s10052-017-5097-x.
14. Nojiri, S.; Odintsov, S.D.; Paul, T. Different faces of generalized holographic dark energy. *Symmetry* **2021**, *13*, 928. https://doi.org/10.3390/sym13060928.
15. 't Hooft, G. Dimensional reduction in quantum gravity. *arXiv* **1993**, arXiv:gr-qc/9310026.
16. Susskind, L. The world as a hologram. *J. Math. Phys.* **1995**, *36*, 6377–6396. https://doi.org/10.1063/1.531249.
17. Cohen, A.G.; Kaplan, D.B.; Nelson, A.E. Effective field theory, black holes, and the cosmological constant. *Phys. Rev. Lett.* **1999**, *82*, 4971–4974. https://doi.org/10.1103/PhysRevLett.82.4971.
18. Li, M. A model of holographic dark energy. *Phys. Lett. B* **2004**, *603*, 1–5. https://doi.org/10.1016/j.physletb.2004.10.014.
19. Hsu, S.D.H. Entropy bounds and dark energy. *Phys. Lett. B* **2004**, *594*, 13–16. https://doi.org/10.1016/j.physletb.2004.05.020.
20. Gao, C.; Wu, F.; Chen, X.; Shen, Y.G. Holographic dark energy model from Ricci scalar curvature. *Phys. Rev. D* **2009**, *79*, 043511. https://doi.org/10.1103/PhysRevD.79.043511.
21. Abd Elrashied, M.; Aly, A.; Selim, M.M. Holographic dark energy models in LTB inhomogeneous universe. *J. Astrophys. Astron.* **2019**, *40*, 15. https://doi.org/10.1007/s12036-019-9581-6.
22. Nojiri, S.; Odintsov, S.D.; Oikonomou, V.K.; Paul, T. Unifying holographic inflation with holographic dark energy. *Phys. Rev. D* **2020**, *102*, 023540. https://doi.org/10.1103/PhysRevD.102.023540.
23. Nojiri, S.; Odintsov, S.D.; Paul, T. Barrow entropic dark energy. *Phys. Lett. B* **2022**, *825*, 136844. https://doi.org/10.1016/j.physletb.2021.136844.
24. Nojiri, S.; Odintsov, S.D.; Saridakis, E.N. Holographic bounce. *Nucl. Phys. B* **2019**, *949*, 114790. https://doi.org/10.1016/j.nuclphysb.2019.114790.
25. Saridakis, E.N. Barrow holographic dark energy. *Phys. Rev. D* **2020**, *102*, 123525. https://doi.org/10.1103/PhysRevD.102.123525.
26. Ghaffari, S.; Luciano, G.G.; Capozziello, S. Barrow holographic dark energy in the Brans–Dicke cosmology. *Eur. Phys. J. Plus* **2023**, *138*, 82. https://doi.org/10.1140/epjp/s13360-022-03481-1.
27. Ens, P.S.; Santos, A.F. Barrow holographic dark energy: A path to reconstructing $f(R,T)$ gravity. *Eur. Phys. J. C* **2024**, *84*, 1338. https://doi.org/10.1140/epjc/s10052-024-13708-3.
28. Yarahmadi, M.; Salehi, A.; Malekjani, M.; Sethi, S.K. Alleviating the Hubble tension using the Barrow holographic dark energy cosmology with Granda–Oliveros IR cut-off. *Mon. Not. R. Astron. Soc.* **2024**, *534*, 3055–3067. https://doi.org/10.1093/mnras/stae2257.

29. Luciano, G.G.; Paliathanasis, A.; Saridakis, E.N. Constraints on Barrow and Tsallis holographic dark energy from DESI BAO data. *arXiv* **2025**, arXiv:2506.03019.
30. del Campo, S.; Fabris, J.C.; Herrera, R.; Zimdahl, W. Cosmology with Ricci dark energy. *Phys. Rev. D* **2013**, *87*, 123002. https://doi.org/10.1103/PhysRevD.87.123002.
31. Fu, T.-F.; Zhang, J.-F.; Chen, J.-Q.; Zhang, X. Holographic Ricci dark energy: Interacting model and cosmological constraints. *Eur. Phys. J. C* **2012**, *72*, 1932. https://doi.org/10.1140/epjc/s10052-012-1932-2.
32. Cai, R.G.; Tuo, Z.L.; Wu, Y.B.; Zhao, Y.Y. More on QCD ghost dark energy. *Phys. Rev. D* **2012**, *86*, 023511. https://doi.org/10.1103/PhysRevD.86.023511.
33. Papagiannopoulos, G.; Luongo, O.; Leon, G.; Paliathanasis, A. Cosmological phase-space analysis of $f(G)$-theories of gravity. *J. High Energy Astrophys.* **2025**, *47*, 100397. https://doi.org/10.1016/j.jheap.2025.100397.
34. Bogadi, R.S.; Giacomini, A.; Govender, M.; Hansraj, C.; Leon, G.; Paliathanasis, A. Anisotropic spacetimes in $f(G)$-gravity: Bianchi I, Bianchi III and Kantowski-Sachs cosmologies. *Gen. Relativ. Gravit.* **2025**, *57*, 129. https://doi.org/10.1007/s10714-025-03465-3.
35. Arora, S.; Meng, X.-H.; Pacif, S.K.J.; Sahoo, P.K. Effective equation of state in modified gravity and observational constraints. *Class. Quantum Grav.* **2020**, *37*, 205022. https://doi.org/10.1088/1361-6382/aba587.
36. Sahoo, P.K.; Moraes, P.H.R.S.; Sahoo, P.; Bishi, B.K. $f(R,T) = f(R) + \lambda T$ gravity models as alternatives to cosmic acceleration. *Eur. Phys. J. C* **2018**, *78*, 736. https://doi.org/10.1140/epjc/s10052-018-6211-4.
37. Capozziello, S.; De Laurentis, M. Extended Theories of Gravity. *Phys. Rept.* **2011**, *509*, 167–321. https://doi.org/10.1016/j.physrep.2011.09.003.
38. Nojiri, S.; Odintsov, S.D.; Oikonomou, V.K. Modified Gravity Theories on a Nutshell: Inflation, Bounce and Late-time Evolution. *Phys. Rep.* **2017**, *692*, 1–104. https://doi.org/10.1016/j.physrep.2017.06.001.
39. Nojiri, S.; Odintsov, S.D. Introduction to modified gravity and gravitational alternative for dark energy. *Int. J. Geom. Methods Mod. Phys.* **2007**, *4*, 115–146. https://doi.org/10.1142/S0219887807001928.
40. Cai, Y.-F.; Capozziello, S.; De Laurentis, M.; Saridakis, E.N. $f(T)$ teleparallel gravity and cosmology. *Rep. Prog. Phys.* **2016**, *79*, 106901. https://doi.org/10.1088/0034-4885/79/10/106901.
41. Nojiri, S.; Odintsov, S.D. Modified gravity with negative and positive powers of the curvature: Unification of the inflation and of the cosmic acceleration. *Phys. Rev. D* **2003**, *68*, 123512. https://doi.org/10.1103/PhysRevD.68.123512.
42. Cognola, G.; Elizalde, E.; Nojiri, S.; Odintsov, S.D.; Sebastiani, L.; Zerbini, S. A Class of Viable Modified $f(R)$ Gravities Describing Inflation and the Onset of Accelerated Expansion. *Phys. Rev. D* **2008**, *77*, 046009. https://doi.org/10.1103/PhysRevD.77.046009.
43. Nojiri, S.; Odintsov, S.D. Unifying Inflation with ΛCDM Epoch in Modified $f(R)$ Gravity Consistent with Solar System Tests. *Phys. Lett. B* **2007**, *657*, 238–245. https://doi.org/10.1016/j.physletb.2007.10.027.
44. Nojiri, S.; Odintsov, S.D. Modified $f(R)$ Gravity Unifying R^m Inflation with ΛCDM Epoch. *Phys. Rev. D* **2008**, *77*, 026007. https://doi.org/10.1103/PhysRevD.77.026007.
45. Jawad, A.; Tariq, H.; Chaudhary, S.; Wu, Q. Stability and thermodynamic geometry of black hole in generalized entropy framework. *Ann. Phys.* **2025**, *473*, 169875. https://doi.org/10.1016/j.aop.2024.169875.
46. Jahromi, A.S.; Moosavi, S.A.; Moradpour, H.; Morais Graça, J.P.; Lobo, I.P.; Salako, I.G.; Jawad, A. Generalized entropy formalism and a new holographic dark energy model. *Phys. Lett. B* **2018**, *780*, 21–24. https://doi.org/10.1016/j.physletb.2018.02.052.
47. Jawad, A.; Rani, S.; Ashraf, S.; Azhar, N. Barrow holographic dark energy in deformed Hořava–Lifshitz gravity. *Int. J. Geom. Methods Mod. Phys.* **2022**, *19*, 2250112. https://doi.org/10.1142/S0219887822501122.
48. Karami, K.; Abdolmaleki, A. Generalized second law of thermodynamics in $f(T)$ gravity. *J. Cosmol. Astropart. Phys.* **2012**, *2012*, 007. https://doi.org/10.1088/1475-7516/2012/04/007.
49. Bekova, G.; Altaibayeva, A.; Ualikhanova, U.; Chattopadhyay, S. Cosmology of barrow holographic dark energy with generalized infrared cutoffs and validity of the generalized second law of thermodynamics. *Eur. Phys. J. C* **2025**, *85*, 1135. https://doi.org/10.1140/epjc/s10052-025-14843-1.
50. Mathew, T.K.; Praseetha, P. Holographic dark energy and generalized second law. *Mod. Phys. Lett. A* **2014**, *29*, 1450023. https://doi.org/10.1142/S0217732314500230.
51. Honarvaryan, M.; Sheykhi, A.; Moradpour, H. Thermodynamical description of the ghost dark energy model. *Int. J. Mod. Phys. D* **2015**, *24*, 1550048. https://doi.org/10.1142/S0218271815500480.
52. Ohta, N. Dark Energy and QCD Ghost. *Phys. Lett. B* **2011**, *695*, 41–44. https://doi.org/10.1016/j.physletb.2010.11.044.
53. Cai, R.-G.; Tuo, Z.-L.; Zhang, H.-B.; Su, Q. Notes on ghost dark energy. *Phys. Rev. D* **2011**, *84*, 123501. https://doi.org/10.1103/PhysRevD.84.123501.
54. García-Salcedo, R.; Gonzalez, T.; Quiros, I.; Thompson-Montero, M. QCD ghost dark energy cannot (even roughly) explain the main features of the accepted cosmological paradigm. *Phys. Rev. D* **2013**, *88*, 043008. https://doi.org/10.1103/PhysRevD.88.043008.
55. Altaibayeva, A.; Ualikhanova, U.; Umurzakhova, Z.; Chattopadhyay, S. A combined Barrow entropy and QCD ghost mechanism for late-time cosmic acceleration. *Eur. Phys. J. C* **2026**, *86*, 344. https://doi.org/10.1140/epjc/s10052-026-15549-8.

56. Gadbail, G.N.; Chaudhary, H.; Bouali, A.; Sahoo, P.K. Statistical and observation comparison of Weyl-type $f(Q,T)$ models with the ΛCDM paradigm. *Nucl. Phys. B* **2024**, *1009*, 116727. https://doi.org/10.1016/j.nuclphysb.2024.116727.
57. Carloni, S.; Elizalde, E.; Odintsov, S. Conformal transformations in cosmology of modified gravity: The covariant approach perspective. *Gen. Relativ. Gravit.* **2010**, *42*, 1667–1705. https://doi.org/10.1007/s10714-010-0936-1.
58. Spergel, D.N.; Verde, L.; Peiris, H.V.; Komatsu, E.; Nolta, M.R.; Bennett, C.L.; Halpern, M.; Hinshaw, G.; Jarosik, N.; Kogut, A.; et al. First-Year Wilkinson Microwave Anisotropy Probe (WMAP) Observations: Determination of Cosmological Parameters. *Astrophys. J. Suppl. Ser.* **2003**, *148*, 175–194. https://doi.org/10.1086/377226.
59. Saha, S. Fundamentals of Relativistic Cosmology. In *Elements of Cosmological Thermodynamics*; Springer: Berlin/Heidelberg, Germany, 2018. https://doi.org/10.1007/978-3-319-74706-4_1.
60. Weinberg, S. *Gravitation and Cosmology: Principles and Applications of the General Theory of Relativity*; Wiley: Hoboken, NJ, USA, 1972.
61. Bekenstein, J.D. Black holes and entropy. *Phys. Rev. D* **1973**, *7*, 2333–2346. https://doi.org/10.1103/PhysRevD.7.2333.
62. Hawking, S.W. Particle creation by black holes. *Commun. Math. Phys.* **1975**, *43*, 199–220. https://doi.org/10.1007/BF02345020.
63. Barrow, J.D. The area of a rough black hole. *Phys. Lett. B* **2020**, *808*, 135643. https://doi.org/10.1016/j.physletb.2020.135643.
64. Nojiri, S.; Odintsov, S.D.; Faraoni, V. From nonextensive statistics and black hole entropy to the holographic dark universe. *Phys. Rev. D* **2022**, *105*, 044042. https://doi.org/10.1103/PhysRevD.105.044042.
65. Shekh, S.H.; Moraes, P.H.R.S.; Sahoo, P.K. Physical Acceptability of the Renyi, Tsallis and Sharma-Mittal Holographic Dark Energy Models in the $f(T,B)$ Gravity under Hubble's Cutoff. *Universe* **2021**, *7*, 67. https://doi.org/10.3390/universe7030067.
66. Urban, F.R.; Zhitnitsky, A.R. The QCD nature of dark energy. *Nucl. Phys. B* **2010**, *835*, 135–173. https://doi.org/10.1016/j.nuclphysb.2010.04.001.
67. Nojiri, S.; Odintsov, S.D.; Paul, T. Early and late universe holographic cosmology from a new generalized entropy. *Phys. Lett. B* **2022**, *831*, 137189. https://doi.org/10.1016/j.physletb.2022.137189.
68. Favale, A.; Gómez-Valent, A.; Migliaccio, M. Cosmic chronometers to calibrate the ladders and measure the curvature of the Universe. A model-independent study. *Mon. Not. Roy. Astron. Soc.* **2023**, *523*, 3406–3422. https://doi.org/10.1093/mnras/stad1621.
69. Naik, D.M. Confronting holographic dark energy with the latest cosmological data: Tensions and model viability. *Mon. Not. R. Astron. Soc.* **2026**, *547*, 3. https://doi.org/10.1093/mnras/stag365.
70. Padmanabhan, T. Cosmological constant—The weight of the vacuum. *Phys. Rep.* **2003**, *380*, 235–320. https://doi.org/10.1016/S0370-1573(03)00120-0.
71. Tajahmad, B.; Motavalli, H. Phase space of multi-fluid universe in $F(T)$-gravity and some enhancements for the oscillating interaction model. *Eur. Phys. J. C* **2021**, *81*, 69. https://doi.org/10.1140/epjc/s10052-021-08871-w.
72. Osano, B.; Oreta, T. Multi-fluid theory and cosmology: A convective variational approach to interacting dark-sector. *Int. J. Mod. Phys. D* **2019**, *28*, 1950078. https://doi.org/10.1142/S0218271819500780.
73. Chen, S.-H.; Dent, J.B.; Dutta, S.; Saridakis, E.N. Cosmological perturbations in $f(T)$ gravity. *Phys. Rev. D* **2011**, *83*, 023508. https://doi.org/10.1103/PhysRevD.83.023508.
74. Bengochea, G.R.; Ferraro, R. Dark torsion as the cosmic speed-up. *Phys. Rev. D* **2009**, *79*, 124019. https://doi.org/10.1103/PhysRevD.79.124019.
75. Linder, E.V. Einstein's other gravity and the acceleration of the universe. *Phys. Rev. D* **2010**, *81*, 127301. https://doi.org/10.1103/PhysRevD.81.127301.
76. Sahni, V.; Saini, T.D.; Starobinsky, A.A.; Alam, U. Statefinder—A new geometrical diagnostic of dark energy. *JETP Lett.* **2003**, *77*, 201–206. https://doi.org/10.1134/1.1574831.
77. Alam, U.; Sahni, V.; Saini, T.D.; Starobinsky, A.A. Exploring the expanding universe and dark energy using the Statefinder diagnostic. *Mon. Not. R. Astron. Soc.* **2003**, *344*, 1057–1074. https://doi.org/10.1046/j.1365-8711.2003.06871.x.
78. Sahni, V.; Shafieloo, A.; Starobinsky, A.A. Two new diagnostics of dark energy. *Phys. Rev. D* **2008**, *78*, 103502. https://doi.org/10.1103/PhysRevD.78.103502.
79. Tolman, R.C. *Relativity, Thermodynamics, and Cosmology*; Courier Corporation: North Chelmsford, MA, USA, 1987.
80. Wang, A.; Wu, Y. Thermodynamics and classification of cosmological models in the Hořava-Lifshitz theory of gravity. *J. Cosmol. Astropart. Phys.* **2009**, *2009*, 12. https://doi.org/10.1088/1475-7516/2009/07/012.
81. Coley, A.A. Thermodynamics and two-fluid cosmological models. *Astrophys. Space Sci.* **1988**, *140*, 175–184. https://doi.org/10.1007/BF00643541.
82. Prigogine, I.; Geheniau, J.; Gunzig, E.; Nardone, P. Thermodynamics and cosmology. *General. Relativ. Gravit.* **1989**, *21*, 767–776. https://doi.org/10.1007/BF00758981.
83. Wang, B.; Gong, Y.; Abdalla, E. Thermodynamics of an accelerated expanding universe. *Phys. Rev. D* **2006**, *74*, 083520. https://doi.org/10.1103/PhysRevD.74.083520.
84. Gibbons, G.W.; Hawking, S.W. Cosmological event horizons, thermodynamics, and particle creation. *Phys. Rev. D* **1977**, *15*, 2738–2751. https://doi.org/10.1103/PhysRevD.15.2738.

85. Davies, P.C.W. Cosmological horizons and the generalised second law of thermodynamics. *Class. Quantum Gravity* **1987**, *4*, L225. https://doi.org/10.1088/0264-9381/4/6/006.
86. Bekenstein, J.D. Generalized second law of thermodynamics in black-hole physics. *Phys. Rev. D* **1974**, *9*, 3292–3300. https://doi.org/10.1103/PhysRevD.9.3292.
87. Unruh, W.G.; Wald, R.M. Acceleration radiation and the generalized second law of thermodynamics. *Phys. Rev. D* **1982**, *25*, 942–958. https://doi.org/10.1103/PhysRevD.25.942.
88. Wu, S.F.; Wang, B.; Yang, G.H.; Zhang, P.M. The generalized second law of thermodynamics in generalized gravity theories. *Class. Quantum Gravity* **2008**, *25*, 235018. https://doi.org/10.1088/0264-9381/25/23/235018.
89. Saridakis, E.N.; Basilakos, S. The generalized second law of thermodynamics with Barrow entropy. *Eur. Phys. J. C* **2021**, *81*, 644. https://doi.org/10.1140/epjc/s10052-021-09431-y.
90. Chattopadhyay, S.; Ghosh, R. A study of generalized second law of thermodynamics in modified $f(R)$ Hořava–Lifshitz gravity. *Astrophys. Space Sci.* **2012**, *341*, 669–674. https://doi.org/10.1007/s10509-012-1088-4.
91. Bamba, K.; Jamil, M.; Momeni, D.; Myrzakulov, R. Generalized second law of thermodynamics in $f(T)$ gravity with entropy corrections. *Astrophys. Space Sci.* **2013**, *344*, 259–267. https://doi.org/10.1007/s10509-012-1312-2.
92. Praseetha, P.; Mathew, T.K. Entropy of holographic dark energy and the generalized second law. *Class. Quantum Gravity* **2014**, *31*, 185012. https://doi.org/10.1088/0264-9381/31/18/185012.
93. Zubair, M.; Jawad, A. Generalized second law of thermodynamics in $f(T, T_G)$ gravity. *Astrophys. Space Sci.* **2015**, *360*, 11. https://doi.org/10.1007/s10509-015-2527-9.
94. Momeni, D.; Moraes, P.H.R.S.; Myrzakulov, R. Generalized second law of thermodynamics in $f(R, T)$ theory of gravity. *Astrophys. Space Sci.* **2016**, *361*, 228. https://doi.org/10.1007/s10509-016-2784-2.
95. Chokyi, K.K.; Chattopadhyay, S. Testing generalized second law of thermodynamics in cosmological models with bulk viscosity and modified gravity. *Eur. Phys. J. C* **2025**, *85*, 771. https://doi.org/10.1140/epjc/s10052-025-14478-2.
96. Tamayo, D. Thermodynamics of sign-switching dark energy models. *Int. J. Mod. Phys. D* **2026**, *35*, 2550104. https://doi.org/10.1142/S0218271825501044.
97. Pai, V.A.; Nelleri, S.; Mathew, T.K. Dissipative ΛCDM model with causal sign-switching bulk viscous pressure. *Eur. Phys. J. C* **2025**, *85*, 593. https://doi.org/10.1140/epjc/s10052-025-14326-3.
98. Shekh, S.H.; Chirde, V.R.; Sahoo, P.K. Energy conditions of the $f(T, B)$ gravity dark energy model with the validity of thermodynamics. *Commun. Theor. Phys.* **2020**, *72*, 085402. https://doi.org/10.1088/1572-9494/ab95fd.
99. Bamba, K.; Geng, C.-Q. Thermodynamics of cosmological horizons in $f(T)$ gravity. *J. Cosmol. Astropart. Phys.* **2011**, *2011*, 008. https://doi.org/10.1088/1475-7516/2011/11/008.

Disclaimer/Publisher's Note: The statements, opinions and data contained in all publications are solely those of the individual author(s) and contributor(s) and not of MDPI and/or the editor(s). MDPI and/or the editor(s) disclaim responsibility for any injury to people or property resulting from any ideas, methods, instructions or products referred to in the content.